

**Evaluation of correlated Pandora column  $\text{NO}_2$  and *in situ* surface  $\text{NO}_2$   
measurements during GMAP campaign**

Lim-Seok Chang<sup>1</sup>, Donghee Kim<sup>1</sup>, Hyunkee Hong<sup>1</sup>, Deok-Rae Kim<sup>1</sup>, Jeonga Yu<sup>1</sup>,  
Kwangyul Lee<sup>1</sup>, Hanlim Lee<sup>2</sup>, Daewon Kim<sup>2</sup>, Jinkyu Hong<sup>3</sup>, Hyun-Young Jo<sup>4</sup>,  
and Cheol-Hee Kim<sup>4, 5</sup>

<sup>1</sup> *Environmental Satellite Center, National Institute of Environmental Research, Incheon, 22689, Republic of Korea*

<sup>2</sup> *Department of Spatial Information Engineering, Pukyong National University, Busan, 48547, Republic of Korea*

<sup>3</sup> *Department of Atmospheric Sciences, Yonsei University, Seoul, 03722, Republic of Korea*

<sup>4</sup> *Institute of Environmental Studies, Pusan National University, Busan, 46241, Republic of Korea*

<sup>5</sup> *Department of Atmospheric Sciences, Pusan National University, Busan, 46241, Republic of Korea*

---

**Correspondence:**

Cheol-Hee Kim (chkim2@pusan.ac.kr), and Lim-Seok Chang (lschang@korea.kr)

1 **Abstract.**

2 To validate the Geostationary Environment Monitoring Spectrometer (GEMS), the GEMS  
3 Map of Air Pollution (GMAP) campaign was conducted during 2020–2021 by integrating  
4 Pandora Asia Network, aircraft, and *in situ* measurements. In the present study, GMAP-2020  
5 measurements were applied to evaluate urban air quality and explore the synergy of Pandora  
6 column (PC) NO<sub>2</sub> measurements and surface *in situ* (SI) NO<sub>2</sub> measurements for Seosan, South  
7 Korea, where large point source (LPS) emissions are densely clustered. Due to the difficulty  
8 of interpreting the effects of LPS emissions on air quality downwind of Seosan using SI  
9 monitoring networks alone, **we explored the combined analysis of both PC-NO<sub>2</sub> and SI-NO<sub>2</sub>**  
10 **measurements.** Agglomerative hierarchical clustering using vertical meteorological variables  
11 combined with PC-NO<sub>2</sub> and SI-NO<sub>2</sub> yielded three distinct conditions: synoptic wind-dominant  
12 (SD), mixed (MD), and local wind-dominant (LD). These results suggest meteorology-  
13 dependent correlations between PC-NO<sub>2</sub> and SI-NO<sub>2</sub>. Overall, yearly daytime mean (11:00–  
14 17:00 KST) PC-NO<sub>2</sub> and SI-NO<sub>2</sub> statistical data showed good linear correlations ( $R = \sim 0.73$ );  
15 however, the differences in correlations were largely attributed to meteorological conditions.  
16 SD conditions characterized by higher wind speeds and **advected marine boundary layer**  
17 heights suppressed fluctuations in both PC-NO<sub>2</sub> and SI-NO<sub>2</sub>, driving a uniform vertical NO<sub>2</sub>  
18 structure with higher correlations, whereas under LD conditions, LPS plumes were decoupled  
19 from the surface or were transported from nearby cities, weakening correlations through  
20 anomalous vertical NO<sub>2</sub> gradients. **The discrepancies suggest that using either PC-NO<sub>2</sub> or SI-**  
21 **NO<sub>2</sub> observations alone involves a higher possibility of uncertainty under LD conditions or**  
22 **prevailing transport processes.** However, under MD conditions, both pollution ventilation due  
23 to high surface wind speeds and daytime photochemical NO<sub>2</sub> loss contributed to stronger  
24 correlations through a decline in both PC-NO<sub>2</sub> and SI-NO<sub>2</sub> toward noon. Thus, Pandora Asia  
25 Network observations collected over 13 Asian countries since 2021 can be utilized for detailed  
26 investigation of the vertical complexity of air quality, and the conclusions can be also applied  
27 when performing GEMS observation interpretation in combination with SI measurements.

28

29 **1. Introduction**

30 Rapid developments in environmental remote sensing have led to a new era of air quality  
31 observations, and recent hyperspectral data retrieval technologies have allowed for routine and

32 accurate monitoring of air pollutants at high spatial and temporal resolution. In particular, the  
33 Geostationary Environment Monitoring Spectrometer (GEMS), which was launched on  
34 February 18, 2020, measures the total and tropospheric air pollutant columns hourly at spatial  
35 resolutions of  $7 \text{ km} \times 8 \text{ km}$  for gas and  $3.5 \text{ km} \times 8 \text{ km}$  for aerosols (Kim et al., 2020), facilitating  
36 the tracking of pollution transport from local to synoptic scales.

37 Recent studies have revealed the potential of satellite observations to evaluate surface air  
38 quality, particularly in regions with sparse air quality-monitoring networks. The main approach  
39 is to convert column density to surface concentrations using a shape factor of the ratio of the  
40 partial column ( $\Omega_{z_0}$ ) within the lowest layer ( $z_0$ ) to the total column ( $\Omega_{\text{total}}$ ) (Zhao et al., 2019),  
41 as follows:

$$42 \quad S = \frac{\Omega_{z_0}}{\Omega_{\text{total}}} \times \frac{C}{\Delta z_0} ,$$

43 where S, C, and  $\Delta z_0$  are the surface concentration, column density, and lowest layer thickness,  
44 respectively. Acquiring accurate profile shape information is critical for determining the  
45 relationship between the column amount and surface concentration because the shape factor is  
46 spatiotemporally variable. Considering this, numerous studies have obtained close  
47 relationships using chemical transport model simulations, aircraft *in situ* measurements, and  
48 satellite observations with high correlation coefficients (R) of 0.7 or more and used them to  
49 scale up surface  $\text{NO}_2$  to column  $\text{NO}_2$  (Wang and Christopher, 2003; Boersma et al., 2009;  
50 Lamsal et al., 2010). This strong correlation can be explained by the generally uniform  
51 planetary boundary layer height (PBLH), and by aerosol type and abundance, which is also the  
52 case for trace gases.

53 By contrast, the implications of weak correlations between column and surface  
54 measurements remain unclear. Engel-Cox et al. (2004) found a negative correlation of AOD  
55 and surface  $\text{PM}_{2.5}$  in northwestern USA, and explained it based on elevated haze decoupled

56 from the surface. Thompson *et al.* (2019) examined weak correlations between Pandora column  
57 (PC) measurements and surface *in situ* (SI) observations of NO<sub>2</sub> over the Yellow Sea during  
58 the Korea–US air quality (KORUS-AQ) field study, and suggested, as a possible reason, the  
59 transported non-uniform plumes originated in China and Seoul hundreds of meters above the  
60 ground from the surface layer. The estimated surface PM<sub>2.5</sub> concentration was weakly  
61 correlated ( $R = 0.4–0.49$ ) with observed PM<sub>2.5</sub> concentrations in Seoul, because only PBLH  
62 was added to the multi-linear regression model to correlate AOD to surface PM<sub>2.5</sub> (Kim *et al.*,  
63 2021). This effect may be related to the significant impact of long-range transport on PM<sub>2.5</sub>,  
64 with a contribution of up to 39% in Seoul (Lee *et al.*, 2021). Thus, the wide variability in the  
65 degree of correlation between PC-PM and SI-PM is closely related to vertical profile variability  
66 (Flynn *et al.*, 2016).

67 It appears highly probable that several factors are responsible for the correlations between  
68 PC-NO<sub>2</sub> and SI-NO<sub>2</sub>; therefore, it is necessary to improve our understanding of the degree of  
69 correlation through detailed measurements, including column concentration. In this study, we  
70 focused on the impact of meteorology and chemistry on correlation variability using PC, SI  
71 and aircraft measurements, as well as meteorological observations. Understanding vertical  
72 profile variability is also useful for evaluating the effects of various emissions on urban air  
73 quality, particularly in areas neighboring active large point source (LPS) emissions sites.  
74 Quantifying the impact of LPS emissions on downwind cities remains challenging due to the  
75 lack of three-dimensional (3D) measurements. Accurate vertical profile data are also useful for  
76 improving remote sensing retrieval algorithms, because the profile shape contributes to the  
77 conversion of slant column density into vertical column density as part of the air mass factor.  
78 In mid-2019, the Pandonia Global Network (PGN; <https://pandonia-global-network.org>) was  
79 launched, with support from the National Aeronautics and Space Administration (NASA) and  
80 European Space Agency (ESA), to facilitate the validation and verification of low-orbit or

81 geostationary environmental satellites. This network is attempting to expand air quality  
82 monitoring through integration with existing long-term air quality monitoring stations. Since  
83 2020, the National Institute of Environmental Research, Economic and Social Commission for  
84 Asia and the Pacific, and Korea Environment Corporation have been extending the Pandora  
85 Asia Network to include 13 Asian countries, with support from the Korea International  
86 Cooperation Agency. The Pandora Asia Network is expected to be widely used to study urban  
87 air quality in Asia, which is increasingly deteriorating due to rapid economic growth.

88 As part of the GEMS Map of Air Pollution (GMAP) campaign, a suite of Pandora  
89 instruments was deployed in Seosan, a South Korean coastal city, from November 2020 to  
90 January 2021 (GMAP-2020), and we applied GMAP-2020 measurements to explore the  
91 synergy of PC observations when evaluating air quality over Seosan. Further results from this  
92 research project are also reported in this special issue, including GEMS validation and urban  
93 air quality evaluations based on Pandora, aircraft, surface flux, and *in situ* surface chemical  
94 measurements conducted during GMAP-2020.

95

## 96 **2. GMAP-2020 campaign**

97 GEMS was launched on February 19, 2020; it is the first instrument to observe air quality from  
98 a geostationary Earth orbit. GEMS provides hourly air quality data on aerosols and gases at a  
99 spatial resolution of 7 km × 8 km. It is a scanning ultraviolet (UV)-visible spectrometer that  
100 observes key atmospheric constituents including O<sub>3</sub>, NO<sub>2</sub>, CO, SO<sub>2</sub>, CH<sub>2</sub>O, CHOCHO,  
101 aerosols, clouds, and UV indices. This mission heralded a new era of satellite air quality  
102 monitoring and will be joined by NASA's Tropospheric Emissions: Monitoring of Pollution  
103 (TEMPO) and ESA's Sentinel-4 to form the GEO Air Quality Constellation in ~3 years, to  
104 cover the most polluted region in the Northern Hemisphere.

105 During GMAP-2020, Pandora instruments (PA<sub>1</sub>–PA<sub>4</sub>) were deployed near large point

106 sources (LPS<sub>1</sub>–LPS<sub>4</sub>) in Seosan; *in situ* surface air quality monitoring systems (AQM<sub>1</sub>–AQM<sub>6</sub>)  
107 and meteorological observations (Met<sub>1</sub>–Met<sub>3</sub>) were also used in this study (see their locations  
108 in Fig. 1). Aircraft measurements were also used to validate GEMS and diagnose LPSs located  
109 in industrial areas surrounding Seosan. We explored the synergy of Pandora observations and  
110 SI measurements, based on measurements collected during GMAP-2020, by evaluating air  
111 quality in industrial Seosan (where LPSs are densely clustered). We particularly investigated  
112 the impacts of vertical profile and sub-pixel variability for trace gases and aerosols, for further  
113 GEMS validation. All measurement sites for both GMAP-2020 campaigns are indicated in  
114 Figure 1.

115

### 116 **3. Methods**

#### 117 **3.1 Study area**

118 Seosan, the target area of the GMAP-2020 campaign, is a small city with a population of  
119 174,780 in 2017; it is accessed via three expressways to the east and four national highways  
120 cross the city. It is located in midwestern South Korea, and is affected by >300 emissions point  
121 sources including LPSs. Coal-fired power plants including Taean, Dangjin, the Hyundai  
122 Dangjin steelworks, and the Daesan petrochemistry industrial complex (LPS<sub>1</sub>–LPS<sub>4</sub>,  
123 respectively, in Fig. 1) have the highest emissions rates in South Korea. The Hyundai Dangjin  
124 steelworks (LPS<sub>3</sub>) and Taean and Dangjin power plants (LPS<sub>1</sub> and LPS<sub>2</sub>) emit 10.5, 11, and  
125 8.8 Gg of NO<sub>x</sub> per year, respectively. Although Seosan accounts for only 1.8% of the  
126 population of Seoul, its NO<sub>x</sub> emissions (10.2 Gg year<sup>-1</sup>) account for 13.2% of its total NO<sub>x</sub>  
127 emissions. The transportation sector of Seosan is a far greater NO<sub>x</sub> source than the industrial  
128 sector of Seoul (ratio of 99:1); however, within Seosan, the industrial sector is on par with the  
129 transport sector (52:48; <http://airemiss.nier.go.kr>).

130 During the past decade, the annual mean NO<sub>2</sub> level in Seosan has been 17 ppb, which is

131 approximately half of that in Seoul (31.2 ppb). NO<sub>2</sub> exhibits strong seasonal variation, reaching  
132 a minimum in summer and maximum in winter, due to meteorological factors and greater  
133 energy use during winter (Kim and Kim, 2020). Therefore, the timing of the GMAP-2020  
134 campaign was well suited to tracking pollution.

135

### 136 **3.2 Pandora measurements**

137 Pandora measures the UV and visible wavelengths (280–525 nm) of direct sunlight with a  
138 spectral resolution of 0.6 nm, to determine the vertical column density of NO<sub>2</sub>, O<sub>3</sub>, and HCHO  
139 (Herman *et al.*, 2009). For measurements in Dobson units (DU; 1 DU = 26.9 Pmol cm<sup>-2</sup>),  
140 column NO<sub>2</sub> has a very high signal-to-noise ratio (700:1) and very high precision (0.01 DU)  
141 for clear skies (Herman *et al.*, 2009). The vertical column density of NO<sub>2</sub> can be determined  
142 using DOAS software (Van Roozendael and Fayt, 2001). Pandora direct-sun measurements are  
143 advantageous in that the air mass factor is simplified, and therefore is dependent only on the  
144 geography for a known solar zenith angle.

145 Four Pandora instruments were installed at sites to the south of LPSs (Fig. 1) during the  
146 GMAP-2020 campaign, i.e., at Seosan Daehoji, Seosan Dongmun, Seosan City Council, and  
147 Seosan Super Site (PA<sub>1</sub>–PA<sub>4</sub> in Fig. 1). The presence of clouds reduces vertical column density  
148 precision by decreasing the number of photons arriving at Pandora instruments within a fixed  
149 integration time. Therefore, the retrieved Pandora measurements were cloud-screened using an  
150 observed cloud cover of 0.6. Cloud cover was provided by the Korea Meteorological  
151 Administration (KMA), and the precision improvement afforded by cloud screening was  
152 verified by comparing each Pandora-derived vertical column density with the median vertical  
153 column density, with and without cloud screening within the inter-comparison period.

154 At PA<sub>4</sub>, the operating period was extended to cover almost the entire year (November 12,  
155 2020–October 30, 2021) including the GMAP-2020 campaign period, and the Pandora spectra

156 were processed into vertical column density data for trace gases using the standard NO<sub>2</sub>  
157 algorithm in BlickP software provided by PGN (Cede, 2019). The resultant PC-NO<sub>2</sub> data were  
158 obtained from the PGN website (<https://pandonia-global-network.org>) for the 1-year period  
159 from Nov. 12, 2020 to Oct. 30, 2021, and were also used as PC-NO<sub>2</sub> statistics for PA<sub>4</sub>, in this  
160 study.

161

### 162 **3.3 Surface and airborne chemical measurements**

163 Hourly average data for SI-NO<sub>2</sub> over a period of 1 year were obtained from Ministry of  
164 Environment AQM network stations in Seosan: Pandori, Leewon, Taeon, Dongmoon,  
165 Seongyeon, and Daesan (AQM<sub>1</sub>–AQM<sub>6</sub>, respectively, in Fig. 1). The Seosan Super Site  
166 (PA<sub>4</sub>/AQM<sub>1</sub>) provided hourly data for NO and NO<sub>y</sub> via an NO-DIF-NO<sub>y</sub> analyzer (42i-Y;  
167 Thermo Scientific, Waltham, MA, USA), and for PM<sub>2.5</sub> chemical species using an ambient ion  
168 monitor (AIM; URG 9000D, URG Corp., Chapel Hill, NC, USA). Weekly zero and span  
169 checks were conducted for NO<sub>y</sub> calibration, to ensure that differences between checks  
170 remained <3%. Water-soluble ions in aerosol and gaseous species were measured hourly using  
171 an AIM, and ion mass balance was used to ensure data quality under the quality control  
172 procedures of the AQM network installation and operation guidelines (NIER, 2021).

173 Aircraft measurements were conducted during the GMAP-2020 campaign period, and  
174 nine flights were conducted on 8 days (Nov. 26, 27, and 28 and Dec. 1, 6, 8, 9, and 12, 2020).  
175 The horizontal and vertical distributions of NO<sub>2</sub> and O<sub>3</sub> over Seosan were measured during  
176 GMAP-2020 using an NO<sub>2</sub> monitor (T500U; Teledyne, Thousand Oaks, CA, USA) and an O<sub>3</sub>  
177 analyzer (TEI49C; Thermo Scientific) onboard the Cessna Grand Caravan 208 B. These  
178 instruments had response times of <40 and <20 s, and detection limits of 40 ppt and 1 ppb,  
179 respectively. The flight paths included a raster mode over all of Seosan at a height of 500–700  
180 m and a profiling mode from 500 m to 1.5 km over PA<sub>1</sub> and PA<sub>4</sub> (Fig. 2).



181

### 182 **3.4 Meteorological measurements**

183 Ground-based hourly observation data for meteorological variables were obtained from Seosan  
184 Automated Synoptic Observing System (ASOS) stations maintained by the KMA, and wind  
185 and temperature profile data were obtained twice daily (0000 and 1200 UTC) via a rawinsonde  
186 instrument at the Osan World Meteorological Organization upper air measurement station  
187 (47122) near Seosan. Due to time constraints of the sonde measurements, information on PBLH  
188 variation was obtained from Unified Model (UM) simulation results provided on the KMA  
189 website (<https://afso.kma.go.kr>).

190 During the GMAP-2020 campaign, a 3D sonic anemometer (CPEC200; Campbell  
191 Scientific, Logan, UT, USA) was also installed on the rooftop at PA<sub>4</sub> for turbulent flux  
192 measurements at the city–atmosphere interface (Hong *et al.*, 2019). All wind components and  
193 sonic temperatures were measured at a 10 Hz sampling rate, and ground-level sensitive heat  
194 flux was measured directly using a 30 min averaging period. Quality controls such as double  
195 rotation, spike removal, and outlier filtering were also applied.

196

### 197 **3.5 Correlation analyses**

198 We examined the synergy of PC and SI data obtained during the GMAP-2020 campaign, and  
199 combined these measurement data to evaluate air quality in Seosan, South Korea. We attempted  
200 to interpret the meteorological and photochemistry data measured during GMAP-2020, and to  
201 demonstrate that caution is required when attempting to study the vertical structure of air  
202 pollutants using either surface observations or satellite data only, particularly in industrial  
203 areas.

204 First, we examined the combined use of year-long PC-NO<sub>2</sub> and SI-NO<sub>2</sub>  
205 measurements, and investigated the factors modulating their correlation. Numerous studies

206 have examined the correlations between chemical species, including aerosols (Thomson et  
207 al., 2019; Wang et al., 2019; Kim et al., 2012; Jo et al., 2013; Sanchez et al., 1990; Kim et al,  
208 2018). Wang *et al.* (2019) reported that aerosols moderately correlate with NO<sub>2</sub> due to the  
209 frequent occurrence of lifted layers probably related to the transport of pollutants. Jo *et al.*  
210 (2013) differentiated haze types using the trajectory speed and direction and different synoptic  
211 conditions. In this background, we hypothesized that their differences in PC-NO<sub>2</sub> and SI-NO<sub>2</sub>  
212 were due to meteorological conditions, and performed k-means and agglomerative hierarchical  
213 cluster analyses of various meteorological variables. Clustering is the grouping of objects that  
214 are alike and are different from the objects belonging to other clusters. As a first step, k-means  
215 Clustering was applied to find smaller clusters until each object was classified in one cluster.  
216 Subsequently, agglomerative hierarchical steps are applied to make up for the shortcomings of  
217 k-means clustering, in which once merging (or splitting) is done, it can never be undone. More  
218 details are found in Venkat Reddy *et al.* (2017). We used XLSTAT software (Addinsoft, Paris,  
219 France) for the cluster analysis with eight meteorological variables representing local and  
220 synoptic circulations in the cluster analysis: surface wind speed (W<sub>sfc</sub>), 925 hPa temperature  
221 (T<sub>925</sub>), sea level pressure (P<sub>sfc</sub>), pressure tendency (dP<sub>sfc</sub>/dt), 850 hPa wind speed (W<sub>850</sub>)  
222 and its north–south and east–west components (NS<sub>850</sub> and EW<sub>850</sub>), and 500 hPa geopotential  
223 height (GPH<sub>500</sub>). We subtracted 30-day moving averages from all data to account for typical  
224 seasonal variation. Monthly averages were used for PC-NO<sub>2</sub> analysis due to the limited  
225 availability of hourly data.

226 Correlations between PC-NO<sub>2</sub> and SI-NO<sub>2</sub> were analyzed in each meteorological group  
227 and the impact of photochemistry was interpreted based on case-specific features. We also  
228 investigated correlations in association with near-surface micrometeorological variables such  
229 as PBLH in each meteorological group.

230

## 231 4. Results and Discussion

232

### 233 4.1 Correlation analysis results for PC-NO<sub>2</sub> and SI-NO<sub>2</sub>

234 The yearly PC-NO<sub>2</sub> statistics at four Pandora sites (PA<sub>1</sub>–PA<sub>4</sub>) are summarized in Table 1. The  
235 total averaged PC-NO<sub>2</sub> over all sites was 0.45 DU during GMAP-2020, which is well above  
236 the typical values (0.1–0.2 DU) for Anmyeondo (the location is shown in Figure 1), a  
237 representative background site (Herman *et al.*, 2018). Although site PA<sub>3</sub> is located in a rural  
238 area, it nevertheless exhibited the highest PC-NO<sub>2</sub> amounts, suggesting that plumes were  
239 frequently transported from nearby point sources and/or urban areas.

240 Scatter diagrams of hourly PC-NO<sub>2</sub> and SI-NO<sub>2</sub> measurements from Pandora sites PA<sub>1</sub>–  
241 PA<sub>3</sub> (GMAP-2020) and PA<sub>4</sub> (yearly measurement; November 12, 2020–October 30, 2021) are  
242 shown in Fig. 3a. These hourly data had a fair logarithmic relationship ( $R = 0.45$ ), and a  
243 relatively weaker 1:1 linear relationship ( $R = 0.41$ ), where the linear relationship with PC-NO<sub>2</sub>  
244 weakened as SI-NO<sub>2</sub> levels increased. It appears that the SI-NO<sub>2</sub> has a distinct diurnal change  
245 despite the same PC-NO<sub>2</sub>, and higher variable surface NO<sub>2</sub> levels may result from the relatively  
246 weaker linear relationship between PC-NO<sub>2</sub> and SI-NO<sub>2</sub>. To explore these anti-correlation  
247 cases further, we selected the lower and upper bounds of the tendencies; these are plotted in  
248 Fig. 3b, which shows that PC-NO<sub>2</sub> was positively correlated with SI-NO<sub>2</sub> on February 24, 2021  
249 ( $R = 0.88$ ), while a negative correlation occurred on April 21, 2021 ( $R = -0.88$ ), indicating a  
250 wide range of case-specific correlations. **The negative correlation on April 21 (Fig. 3b) implied**  
251 **that the nonhomogeneous NO<sub>2</sub> distributions vertically were partially due to the photochemical**  
252 **process. For example, the decrease in PC-NO<sub>2</sub> despite an increase in SI-NO<sub>2</sub> might have**  
253 **occurred because NO<sub>2</sub> is removed by photochemical loss; it can occur more severely in the**  
254 **upper atmosphere with high OH concentrations. Another possible reason is the occurrence of**  
255 **lifted layers related to pollutant transport, yielding sharp changes in vertical concentration from**

256 the surface to the upper layer. The case-specific discussion follows.

257 Generally, in remote and clean regions such as the Pacific Ocean, local surface NO<sub>2</sub>  
258 concentrations are considered at background level, and can be used to represent stratospheric  
259 NO<sub>2</sub> amounts. The background level in our study would ideally correspond to the intercept of  
260 the regression model in the PC-SI NO<sub>2</sub> scatter diagram (Fig. 3a). In our analysis of yearly  
261 measurements, the intercept of 0.09 DU was consistent with stratospheric NO<sub>2</sub> column density  
262 ( $0.10 \pm 0.02$  DU) estimated during the GMAP campaign from the tropospheric monitoring  
263 instrument (TROPOMI) at a nadir pass time of approximately at 1330.

264

#### 265 **4.2 Impacts of meteorological conditions on correlations between PC-NO<sub>2</sub> and SI-NO<sub>2</sub>**

266 Our k-means cluster analysis distinguished three groups with the lowest within-group variance  
267 and largest among-group variance. Among the total of 141 cases, 47, 66, and 28 were classified  
268 into groups 1–3, respectively. Thus, group 2 had the largest proportion of cases (47%) and  
269 group 3 had the smallest (20%). The combination of meteorological components in group 1  
270 indicated the end of a high-pressure system ( $P_{sfc} > 0$ ,  $dP_{sfc}/dt < 0$ ), with southerly winds  
271 ( $NS850 > 0$ ) bringing warmer air ( $T925 > 0$ ) to the region, leading to stable atmospheric  
272 stratification and weak surface winds (Fig. 4). This group 1 meteorological mode appeared to  
273 result in very weak NO<sub>2</sub> ventilation, which produced the highest PC-NO<sub>2</sub> and SI-NO<sub>2</sub> values.  
274 Group 3 showed the opposite trend, with strong northerly winds bringing colder air into the  
275 region, leading to an unstable atmosphere and stronger surface winds, and ultimately  
276 decreasing PC-NO<sub>2</sub> and SI-NO<sub>2</sub> to their lowest levels.

277 SI-NO<sub>2</sub> was approximately twice as high in group 1 than group 3, whereas PC-NO<sub>2</sub>  
278 showed no significant difference (Fig. 4a). We hypothesized that PBLH might also differ  
279 significantly under these micrometeorological conditions; therefore, we further explored daily  
280 maximum PBLH simulated by the Global Forecast System (GFS) and Lagrangian backward

281 trajectories obtained from Hybrid Single-Particle Lagrangian Integrated Trajectory  
 282 (HYSPLIT) and GFS system for the 141 cases. The mean simulated PBLH in Seosan, our study  
 283 area, was  $942.1 \pm 405.3$  m for 2020, which was similar to the annual mean daily maximum  
 284 PBLH (1,013.6 m) in Osan (Lee *et al.*, 2013). However, the simulated PBLH differed  
 285 significantly among the three groups ( $767.0 \pm 304.8$ ,  $923.2 \pm 335.3$ , and  $1,280.6 \pm 501.2$  m for  
 286 groups 1–3, respectively). The PBLH for group 3 was 1.7-fold higher than that for group 1  
 287 (Fig. 4k). We also detected significant differences among the three groups in synoptic  
 288 components of the lower troposphere including W850, as well as in local meteorological  
 289 parameters such as the sea breeze index (SBI) suggested by Biggs and Graves (1962), which  
 290 is defined as,  $SBI = \frac{U^2}{C_p \Delta T}$ , where  $U$  is Wsfc (Fig. 4c),  $C_p$  is specific heat, and  $\Delta T$  is the  
 291 temperature difference between T925 and the sea surface temperature. Thus, the SBI represents  
 292 the ratio between inertial ( $\rho U^2/2$ ) and buoyance forces ( $\rho g C_p \Delta T$ ), where  $\rho$  is air density and  $g$   
 293 is gravity, and its value provides an indication of the likelihood of local circulation events such  
 294 as sea breezes; at higher SBIs (i.e.,  $SBI > 3$ ), sea breezes cannot overcome the prevailing wind,  
 295 whereas lower SBIs (i.e.,  $0 < SBI < 3$ ) can indicate strong sea breezes.

296 In the example shown in Fig. 4l, the SBI for groups 1–3 was  $0.1 \pm 4.5$ ,  $0.1 \pm 9.2$ , and  $-0.2$   
 297  $\pm 12.5$ , respectively. Most SBIs in group 1 ranged from 0 to 3, indicating that group 1  
 298 corresponded to the dominant local circulation (LD), whereas the SBIs in group 3 had the  
 299 lowest frequencies comparing 1 and 3, which corresponded to a dominant synoptic-scale  
 300 circulation (SD). Group 2 can be considered a mixture of local and synoptic-scale circulation  
 301 (MD). These results indicate that Seosan may experience frequent LD conditions (with sun on  
 302 one third of the days of the year), with infrequent SD conditions (one fifth of all days).

303

#### 304 4.2.1 Relationship between daily mean PC-NO<sub>2</sub> and SI-NO<sub>2</sub> under LD, MD, and SD

305 **conditions**

306 Scatter diagrams of daytime mean PC-NO<sub>2</sub> and SI-NO<sub>2</sub> measurements at Seosan over the entire  
307 1-year period are shown in Fig. 5. Based on the 141 cases, daytime mean values averaged  
308 between 1100 and 1700 KST were used to reduce the effect of nocturnal PBLH variation. Other  
309 data selection criteria included concurrent PC-NO<sub>2</sub> and SI-NO<sub>2</sub> measurements, with data  
310 acquisition rates of >80% per day. Overall, PC-NO<sub>2</sub> and SI-NO<sub>2</sub> were strongly correlated ( $R =$   
311 0.73; Fig. 5), suggesting that the vertical profiles were generally uniform in the PBL throughout  
312 all four seasons. The slope of the linear regression curve shown in Fig. 5a was 0.02 DU/ppb (=  $0.53 \times 10^{15}$   
313 molecules cm<sup>-2</sup>/ppb), which is comparable to values ( $0.3\text{--}0.59 \times 10^{15}$  molecules  
314 cm<sup>-2</sup>/ppb) obtained previously in a study of surface and OMI-NO<sub>2</sub> measurements downwind  
315 of strong point sources in Israeli cities (Boersma *et al.*, 2009). The intercept (0.17 DU) was  
316 within the range of previous Anmyeondo Pandora measurements, suggesting that intercepts of  
317 0.15–0.2 DU may represent the local background PC-NO<sub>2</sub> amount (including the stratospheric  
318 NO<sub>2</sub>), rather than the influence of local anthropogenic NO<sub>2</sub> emissions.

319 We classified daily averaged PC-NO<sub>2</sub> and SI-NO<sub>2</sub> data according to the three  
320 meteorological conditions (LD, MD, and SD) and detected a weak correlation under LD  
321 conditions (Fig. 5b); the lowest coefficient of determination for the LD condition ( $R^2 = 0.34$ )  
322 was approximately half of those for the MD (0.359) and SD (0.64) conditions, suggesting that  
323 NO<sub>2</sub> vertical profiles were more complex under LD conditions, with anomalous layers.

324

#### 325 **4.2.2 Diurnal variation in column-surface NO<sub>2</sub> under LD, MD, and SD conditions**

326 Diurnal patterns of PC-NO<sub>2</sub>, SI-NO<sub>2</sub>, and O<sub>3</sub> under SD, MD, and LD conditions are shown in  
327 Fig. 6. Under LD conditions, PC-NO<sub>2</sub> increased from morning to afternoon (Fig. 6a), whereas  
328 under SD conditions, it had a weak morning peak and subsequent decrease until late afternoon  
329 (Fig. 6c). Under MD conditions, PC-NO<sub>2</sub> had one large peak in the morning and a shoulder

330 peak in the late afternoon (Fig. 6b). However, SI-NO<sub>2</sub> showed nearly identical diurnal patterns  
331 among the three meteorological conditions, with an early morning peak followed by a second  
332 peak in the late afternoon (Fig. 6d–f). Diurnal patterns of O<sub>3</sub> were strongly associated with O<sub>3</sub>-  
333 NO<sub>2</sub> photochemical reactions under both LD and MD conditions (Fig. 6g–h), whereas no  
334 particular photochemical effects were detected under SD conditions (Fig. 6i).

335 A simple linear regression was applied to daytime average (1100–1700 LST)  
336 measurements of both PC-NO<sub>2</sub> and SI-NO<sub>2</sub> under the three meteorological conditions, and  
337 yielded correlation coefficients ( $R$ ) of 0.51 and 0.41 for SD and MD conditions, respectively;  
338 however, LD conditions produced a significantly lower  $R$  (0.27). Thus, under SD conditions,  
339 strong synoptic winds suppressed PC-NO<sub>2</sub> and SI-NO<sub>2</sub> diurnal fluctuations, rendering them  
340 similar to each other. Strong winds also inhibited local effects of O<sub>3</sub> formation on the diurnal  
341 variation in PC-NO<sub>2</sub>, and the smaller impact of chemical conversion from local NO<sub>2</sub> to O<sub>3</sub>  
342 lowered  $R$  values during the day. Under MD conditions, both PC-NO<sub>2</sub> and SI-NO<sub>2</sub> exhibited  
343 distinctive peaks in the morning with a degree of time lag; both subsequently declined toward  
344 noon, and showed higher  $R$  values than those obtained under SD conditions. By contrast, under  
345 MD conditions, correlations were enhanced due to a minimum around 1500 KST for both PC-  
346 NO<sub>2</sub> and SI-NO<sub>2</sub>, despite time lags in both peaks in the morning and afternoon.

347 Previous studies of the Megacity Air Pollution Seoul (MAPS-Seoul) and KORUS-AQ  
348 campaigns reported a typical pattern of continuously increasing PC-NO<sub>2</sub> over the Seoul  
349 metropolitan area (Chong *et al.*, 2018; Herman *et al.*, 2018). However, in the current  
350 campaign, we found similar results only under LD conditions. The diurnal patterns reported in  
351 previous studies were mainly caused by the dominance of NO<sub>2</sub> emissions sources over NO<sub>2</sub>  
352 losses (Chong *et al.*, 2018; Herman *et al.*, 2018) among several processes associated with NO<sub>2</sub>  
353 photochemical loss, including transport and deposition, which were also investigated in  
354 specific cases in the current study.

355 In this study, we extended the correlation analysis, and investigated the correlation  
356 between hourly PC-NO<sub>2</sub> and SI-NO<sub>2</sub> data. The results show a lower correlation in the morning,  
357 and a higher correlation in the afternoon (Fig. S1). The respective median correlation  
358 coefficients for the LD, MD, and SD meteorological conditions were -0.71, 0.18, and 0.22 in  
359 the morning (0900–1200 LST), and 0.84, 0.77, and 0.79 in the afternoon (1200–1400 LST).  
360 These values may reflect PBL development. SI-NO<sub>2</sub> decreases in the morning due to the rapid  
361 growth of the PBL, while PC-NO<sub>2</sub> increases due to the accumulation of NO<sub>2</sub> in the atmosphere,  
362 deriving a lower correlation. However, there is very little change in the PBL in the afternoon,  
363 and PC-NO<sub>2</sub> and SI-NO<sub>2</sub> show similar changes, yielding a positive correlation each other  
364 during the GMAP-2020 campaign.

365

#### 366 **4.3 Aircraft measurements collected during GMAP-2020**

367 Data collected via aircraft during GMAP-2020 are summarized in Table 2. A total of nine  
368 aircraft measurements were conducted during the campaign period (November 12, 2020–  
369 January 20, 2021). Four of nine flights were conducted under LD conditions, and the remaining  
370 flights (except that on November 27, 2020) were conducted under MD conditions. No aircraft  
371 measurements were consistent with SD conditions during the GMAP-2020 campaign.

372 We examined spiral segments from each flight over Seosan during 1100–1700KST to  
373 exclude marginal effects of diurnal variation in NO<sub>2</sub> (Fig. 2). The overall results indicated that  
374 the vertical O<sub>3</sub> profiles were relatively constant in the PBL, whereas NO<sub>2</sub> profiles appeared to  
375 be highly dependent on meteorological conditions. We compared data collected during flights  
376 conducted under LD (one flight) and MD conditions (two flights) during the GMAP-2020  
377 campaign, to examine differences in the vertical structures of the PA and SI observations.  
378 Aircraft measurements of vertical NO<sub>2</sub> and O<sub>3</sub> profiles for flights FL-5 (December 6) and FL-  
379 6 (December 8) under LD conditions are shown in Fig. 7, along with 24 h backward trajectories



380 starting at different altitudes (100, 500, and 1,000 m). All observed NO<sub>2</sub> profiles shown in Fig.  
381 7 appeared to have generally exponential curves, with anomalous features at higher altitudes.  
382 For example, when vertical turbulent mixing prevailed within the PBL (O<sub>3</sub> profile, Fig. 7b),  
383 the data were fitted with an exponential vertical curve, and the anomalous NO<sub>2</sub> layer aloft was  
384 found to have a height of 1.5 km, which was higher than the estimated PBLH of 1.2 km.  
385 HYSPLIT 24 h backward trajectories starting at 1200 KST showed that all air mass from the  
386 surface to the lower free atmosphere was transported over the Yellow Sea via the Shandong  
387 Peninsula (Fig. 7c). This finding suggests that the anomalous NO<sub>2</sub> layer aloft was not produced  
388 locally (i.e., from local LPS emissions), but instead traveled via long-range regional-scale  
389 transport. **This transport of NO<sub>2</sub> across the region was also discussed and might be particularly**  
390 **high during the winter when the NO<sub>x</sub> lifetime is relatively longer (Stohl *et al.*, 2002; Wenig *et***  
391 ***al.*, 2003; Lee *et al.*, 2013).** According to Anmyeondo Lidar measurements for December 6  
392 (<http://kalion.kr>), the anomalous NO<sub>2</sub> layer aloft corresponded well to an aerosol layer that  
393 appeared at ~1.0 km at approximately 1200 KST, persisting until 2200 KST. However, based  
394 on a cross-comparison of our data, high surface levels of SI-NO<sub>2</sub> (> ~4 ppb; Fig. 7a) were  
395 influenced more by local LPS than by that in the atmosphere aloft due to long-range transport  
396 (Fig. 7a).

397 Aircraft measurements for flight FL-7 (December 9) under LD conditions are shown in  
398 Fig. 7b. The NO<sub>2</sub> vertical profile exhibited an exponential curve, with an anomalous peak at  
399 ~600 m immediately above the top of the simulated PBL. HYSPLIT backward trajectory data  
400 starting at 1200 KST showed that the non-surface air had a different origin from the surface air  
401 (Fig. 6d), indicating that the anomalous NO<sub>2</sub> plume likely traveled from coal-fired power plants  
402 in a nearby industrial city (Taean) northwest of Seosan. This finding indicates a distinct vertical  
403 structure of higher NO<sub>2</sub> at the surface due to strong local emissions, whereas lower NO<sub>2</sub> levels  
404 were observed at higher altitudes, with anomalously high NO<sub>2</sub> levels in some layers aloft due

405 to medium-range transport from nearby areas. Thus, despite the limited number of aircraft  
406 measurements, the elevated anomalous NO<sub>2</sub> structure that was observed intermittently led to a  
407 negative correlation between PA-NO<sub>2</sub> and SI-NO<sub>2</sub>. **The discrepancies imply that vertical  
408 profile distribution study should proceed cautiously when only surface measurements are  
409 obtained under LD meteorological conditions.**

410 Aircraft measurements were conducted under MD conditions on flights FL-1 (November  
411 26), FL-3 (November 28), and FL-8 (December 12) (Fig. 8). We applied several regression  
412 models (linear, exponential, and polynomial) to three vertical structures, and obtained two  
413 distinct NO<sub>2</sub> vertical profile patterns from the surface to the PBLH: decreasing linearly for FL-  
414 1 and FL-8 (Fig. 8), and constant with altitude for FL-3 (Fig. 8b). None of the three cases  
415 showed anomalous layers above the PBLH, similar to the exponentially declining profiles  
416 obtained under LD conditions (Fig. 7). These vertical structures observed under MD conditions  
417 may have been induced by strong vertical mixing within the PBL, supplemented by prominent  
418 surface photochemical losses at the same time. The vertical O<sub>3</sub> profile during FL-1 showed a  
419 decoupled structure, with different patterns within and above the PBL (Fig. 8d); however, the  
420 other 2 days showed uniform distributions, with no particular anomalous features between the  
421 upper PBL and surface atmosphere (Fig. 8b, c, e, f). The observed daily maximum sensible  
422 heat fluxes measured at Seosan (Fig. S3) were much higher for FL-3 (175.9 Wm<sup>-2</sup>) than FL-1  
423 and FL-8 (118.9 and 102.0 Wm<sup>-2</sup>), suggesting that vertical turbulent mixing was much more  
424 prominent during FL-3. These chemical and physical characteristics are all related to MD  
425 conditions. Thus, the higher coefficient of determination ( $R^2 = 0.64$ ) obtained under MD  
426 conditions (Fig. 5b) has an important bearing on the absence of irregular or anomalous layers  
427 aloft, with little variation regardless of the shape of the curve (Figs. 7 and 8).

428

#### 429 **4.4 Analyses of column–surface relationships for specific GMAP-2020 cases**

430 Figure 9 shows examples of PC-NO<sub>2</sub> and SI-NO<sub>2</sub> diurnal variation under LD (FL-5 and FL-7)  
431 and MD (FL-1 and FL-8) conditions, and Fig. 10 shows latitudinal mean distributions for FL-  
432 5 and FL-7, based on the aircraft measurement data shown in Figs. 7 and 8. PC-NO<sub>2</sub> was  
433 decoupled from SI-NO<sub>2</sub> on 2 days, FL-5 and FL-7, which were both classified as having LD  
434 conditions (Fig. 9a, b), whereas good vertical mixing and uniform NO<sub>2</sub> distribution were  
435 observed on the remaining 2 days, FL-1 and FL-8, which showed MD conditions (Fig. 9c, d).  
436 According to our analysis of the aircraft measurements (Fig. 7), the poor correlations between  
437 PC-NO<sub>2</sub> and SI-NO<sub>2</sub> captured by FL-5 and FL-7 were mainly due to an NO<sub>2</sub> polluted layer  
438 transported aloft, as described in Section 4.3.

439

#### 440 **4.4.1 LD conditions**

441 Several cases showed poor correlations between PC-NO<sub>2</sub> and SI-NO<sub>2</sub> under LD conditions  
442 within the study period. When we examined the results of previous studies (Thompson et al.,  
443 2019; Chong et al., 2018; Herman et al., 2018; Kim et al., 2021), we first considered the  
444 possibility that LPS emissions influenced downwind regions under LD conditions, because the  
445 increase in PC-NO<sub>2</sub>, but not SI-NO<sub>2</sub>, may have required an additional source of NO<sub>2</sub> apart from  
446 early afternoon traffic emissions. The FL-5 data for December 6 represent an example of this,  
447 showing a poor correlation between PC-NO<sub>2</sub> and SI-NO<sub>2</sub> ( $R^2 = 0.06$ ; Fig. 9a). On the same day,  
448 Anmyeondo LIDAR detected two elevated aerosol layers at 1200 and 1600–2200 KST  
449 (<http://kalion.kr>); the first aerosol layer may reflect a PC-NO<sub>2</sub> peak, as shown in Fig. 9a. The  
450 HYSPLIT backward trajectories, starting at different altitudes from the surface to the lower  
451 troposphere, revealed that all air parcels moved eastward from China to Anmyeondo and  
452 Seosan (Figure 1); thus, other NO<sub>2</sub> plumes may have begun to pass over Seosan at 1600KST  
453 (Fig. 7c). Longitudinal SI-NO<sub>2</sub> distributions (Fig. 10) exhibited 5.2 ppb at 126.1°E, 8.1 ppb at  
454 126.3°E, and 7.3 ppb at 126.4°E, averaged between 1300 and 1600 KST by longitude (Table

455 S1), whereas they were nearly constant at a height of 500–600 m on December 6. Therefore,  
456 westerly winds advected cleaner air from Padori (AQM<sub>1</sub>) to Seosan at the surface, but not at a  
457 height of 500–600 m, contributing to low SI-NO<sub>2</sub> levels in the afternoon (Fig. 9a).

458 Another example of a weak correlation was obtained by flight FL-7 (December 9), as  
459 shown in Fig. 9b. Time series PC-NO<sub>2</sub> data exhibited several peaks during 1200–1400 KST  
460 (Fig. 9b), whereas SI-NO<sub>2</sub> showed less temporal variation, resulting in a weak correlation ( $R =$   
461  $-0.24$ ) compared to the overall daytime (1100–1700 KST) correlation ( $R^2 = 0.53$ ; Fig. 5a).  
462 Latitudinal NO<sub>2</sub> levels at high altitudes of ~600 m (Fig. 10b) gradually increased northward,  
463 whereas surface NO<sub>2</sub> was minimal at the midpoint. For example, at high altitudes, the  
464 latitudinal mean NO<sub>2</sub> levels were 1.4 ppb (36.8°N), 4.1 ppb (36.9°N), and 5.1 ppb (37.0°N),  
465 whereas the SI-NO<sub>2</sub> levels at the same sites were 18.0 ppb (36.8°N), 14.3 ppb (36.9°N), and  
466 16.8 ppb (37.0°N), respectively, averaged during 1200–1400 KST by latitude (Table S1). This  
467 finding is attributable to a prevailing north wind that transported NO<sub>2</sub> southward at high  
468 altitudes, while simultaneously ventilating SI-NO<sub>2</sub> toward outer Seosan, resulting in the  
469 development of several PC-NO<sub>2</sub> peaks. By contrast, SI-NO<sub>2</sub> decreased slowly (Figs. 9b and  
470 10b).

471

#### 472 **4.4.2 MD and SD conditions**

473 We obtained higher PC–SI correlation coefficients under MD and SD conditions than LD  
474 conditions (Figs. 5b and 9c, d). Under MD and SD conditions, diurnal variation in PC-NO<sub>2</sub> and  
475 SI-NO<sub>2</sub> showed simultaneous declines from early morning until noon (Fig. 6). Notably, PC-  
476 NO<sub>2</sub> showed a continuously decreasing trend, particularly during the morning hours, in the  
477 period of approximately 0900–1200 KST under both MD and SD conditions (Fig. 6b, c). These  
478 diurnal patterns of decreasing PC-NO<sub>2</sub> in the study area were opposite to those reported in  
479 previous studies (Chong *et al.*, 2018; Herman *et al.*, 2018) that observed increasing PC-NO<sub>2</sub> in

480 large urban areas during the daytime, caused by higher NO<sub>2</sub> emissions even during  
481 photochemical NO<sub>2</sub> losses to form O<sub>3</sub>.

482 We hypothesized that decreasing PC-NO<sub>2</sub> can occur due to photochemical loss and  
483 surface wind transport, which both intensify with increasing solar radiation in the morning.  
484 Photochemically, NO<sub>2</sub> is converted into photochemical oxidants such as PAN, HNO<sub>3</sub>, and  
485 nitrate under sunlight, thereby disrupting the NO<sub>x</sub>-VOC-O<sub>3</sub> cycle. Concurrently, W<sub>sf</sub>c  
486 intensified due to thermal turbulence transport of NO<sub>2</sub> emissions away from Seosan during the  
487 day. Thus, PC-NO<sub>2</sub> decreases under MD conditions as a result of ventilation effects caused by  
488 stronger wind speeds. There are two possible mechanisms for this: sea breeze penetration  
489 (because the study area is adjacent to the northern coast of the Taean Peninsula; Fig. 1) and  
490 vigorous turbulent mixing (which leads to vertical mixing of surface NO<sub>2</sub> during PBL growth;  
491 Sun *et al.*, 2013). We investigated these factors in detail for specific cases.

492 Figure 11 shows the diurnal variation in selected meteorological and chemical variables  
493 measured under MD (November 25) and SD conditions (December 14). Under MD conditions  
494 (Fig. 11a–c), declines in PC-NO<sub>2</sub> and SI-NO<sub>2</sub> were observed toward noon. In particular,  
495 decreasing PC-NO<sub>2</sub> was accompanied by increased W<sub>sf</sub>c (Fig. 11b); therefore, we examined  
496 GMAP-2020 campaign measurements of sea breeze penetration. Figure S2a shows diurnal  
497 variation in observed air temperatures at site Met<sub>1</sub> and measured sea surface temperatures at  
498 nearby site Met<sub>2</sub> (37.14°N, 126.01°E), located 55 km from PA<sub>4</sub>. The thermal meteorological  
499 observations were used to calculate SBI (+0.37), which was greater than +3 (the threshold for  
500 sea breeze occurrence; Brigges and Graves, 1962). Sea breeze disturbances with a sharp  
501 decrease (increase) in temperature (humidity) were observed at site Met<sub>3</sub> (Fig. S3b), which is  
502 located on the northern coastline of Taean Peninsula (Fig. 1). However, sea breezes did not  
503 progress inland at the Met<sub>1</sub> Seosan Meteorological Automated Surface Observing System  
504 (ASOS) site, which is closer to the Pandora sites; sea breezes did not correlate with NO<sub>2</sub>

505 ventilation to offset its high emission.

506 We further detected a strong positive correlation between wind speed and sensible heat  
507 flux (Fig. 11b). We speculated that thermal and momentum turbulences caused by a vertical  
508 temperature gradient and surface friction entrained surface turbulence, thus increasing  
509 momentum in the free atmosphere downward to the surface due to strong turbulent mixing  
510 within the PBL, in turn leading to a uniform vertical NO<sub>2</sub> profile with a positive correlation  
511 between PC-NO<sub>2</sub> and SI-NO<sub>2</sub>. Figure S3 shows a comparison of daily maximum sensible heat  
512 and momentum fluxes under LD, MD, and SD conditions during the GMAP-2020 campaign.  
513 SD conditions showed the highest mean heat flux, followed by MD and LD, indicating that  
514 downward momentum transport led by both heat and momentum fluxes plays a greater role in  
515 Wsfc enhancement under MD than LD conditions within the PBL.

516 Photolytic NO<sub>2</sub> loss was detected as temporal variation in NO<sub>2</sub>, NO<sub>3</sub><sup>-</sup>, and CO at PA<sub>4</sub>.  
517 Because no NO<sub>2</sub> analyzer was installed at PA<sub>4</sub>, NO<sub>2</sub><sup>\*</sup>(= NO<sub>y</sub>-NO) was used instead of NO<sub>2</sub>  
518 under the assumption that NO<sub>z</sub> is negligible in winter. Figure 11c shows the diurnal variation  
519 in NO<sub>2</sub>, O<sub>3</sub>, and NO<sub>3</sub><sup>-</sup> under MD conditions, normalized by CO to reduce the effect of PBL  
520 evolution. The results showed that NO<sub>2</sub>/CO decreased after the morning peak; however, NO<sub>3</sub><sup>-</sup>  
521 /CO and O<sub>3</sub>/CO increased toward midday, indicating that photolytic activity also contributed  
522 considerably to the concurrent decline of SI-NO<sub>2</sub> and PC-NO<sub>2</sub> (Fig. 11a). In turn, this indicated  
523 that photochemistry can contribute to higher correlation coefficients under MD conditions.

524 Under SD conditions (Fig. 11d-f), PA-NO<sub>2</sub> and SI-NO<sub>2</sub> exhibited weak diurnal variability  
525 compared to LD and MD conditions. SD conditions on December 14 produced significantly  
526 stronger winds (i.e., wind speed > 6 m s<sup>-1</sup> at 1300 KST), with generally higher PBLHs (Fig.  
527 11e). Meteorological features, such as strong wind at both 850 hPa (18.0 m s<sup>-1</sup>) and 10 m height  
528 (4.26 m s<sup>-1</sup>), suppressed both PC-NO<sub>2</sub> and SI-NO<sub>2</sub> (7.3 ppb and 0.31 DU, respectively) to  
529 below the average, producing a strong correlation ( $R = 0.9$  at AQM<sub>5</sub>) and nearly flattening their

530 temporal curves during the day (Fig. 11d). Thus, under SD conditions, wind speed and  
531 turbulent fluxes such as sensible heat flux had larger values, and  $\text{NO}_2$  and  $\text{NO}_3^-$  decreased or  
532 increased at the same time during the day (Fig. 11f), indicating that the transport effect was  
533 much greater than that of local photochemical loss over the study area.

534 In conclusion, in this case-specific study, we assessed the correlations between PC- $\text{NO}_2$   
535 and SI- $\text{NO}_2$ , and explored their mechanisms by investigating the impact of meteorological and  
536 photochemical conditions. A weak correlation between PC- $\text{NO}_2$  and SI- $\text{NO}_2$  occurred when  
537 anomalously high concentrations remained, with ragged fragments of  $\text{NO}_2$  plumes in the upper  
538 or middle layers. We also found that a negative correlation occurred intermittently under LD  
539 conditions, with generally lower PBLH. In particular, elevated pollutant levels due to regional-  
540 scale transport or decoupled  $\text{NO}_2$  plumes advected within the PBL may have also caused the  
541 weak correlation between PC- $\text{NO}_2$  vs. SI- $\text{NO}_2$ . These phenomena were detected only from the  
542 PA-SI coupled measurements in this study. Thus, when either PC or SI observations are  
543 applied alone for understanding the vertical structure of air pollutants, undetected bias can  
544 occur under LD conditions, particularly where transport processes prevail, and these results  
545 can be also applicable to GEMS observations analysis.

546

## 547 **5. Conclusion**

548 We explored the potential applicability of combined PC- $\text{NO}_2$  and SI- $\text{NO}_2$  measurements  
549 collected at Seosan during the GMAP-2020 campaign. We characterized the correlation  
550 between PC- $\text{NO}_2$  and SI- $\text{NO}_2$  under various conditions to understand the complex air quality  
551 of Seosan, which appears to be vulnerable to LPS emissions from surrounding areas. We  
552 hypothesize that correlations between PC- $\text{NO}_2$  and SI- $\text{NO}_2$  are closely related to  $\text{NO}_2$  vertical  
553 profiles, which also depend on meteorological conditions. We performed statistical analyses of  
554 a year-long PC- $\text{NO}_2$  dataset (November 12, 2020–October 30, 2021) combined with

555 meteorological data, *in situ* ground data, and airborne chemical data measured during the  
556 GMAP-2020 campaign in the same period.

557 Our results show that hourly PC-NO<sub>2</sub> and SI-NO<sub>2</sub> over the 1-year period exhibited a  
558 logarithmic relationship with a fair correlation ( $R = 0.45$ ), and the intercept of the logarithm  
559 regression line (corresponding to zero-surface NO<sub>2</sub>) was 0.09 DU, consistent with the  
560 stratospheric column NO<sub>2</sub> amounts retrieved by TROPOMI. Daily mean PC-NO<sub>2</sub> and SI-NO<sub>2</sub>  
561 exhibited a good linear correlation ( $R = 0.73$ ), supporting the overall uniformity of NO<sub>2</sub> profiles  
562 in the PBL over Seosan despite the continuous impact of LPS emissions.

563 The impact of meteorological conditions on the relationship between PC-NO<sub>2</sub> and SI-NO<sub>2</sub>  
564 was investigated through agglomerative hierarchical clustering, which indicated three  
565 meteorological conditions: LD, MD, and SD. Under LD conditions, southerly winds advect  
566 warm air under the upper ridge, forming stable and short PBLs and weak surface winds. By  
567 contrast, under SD conditions, cold northerly winds induce unstable and high PBLs with strong  
568 surface winds. The correlations between daily mean PC-NO<sub>2</sub> and SI-NO<sub>2</sub> levels, and their  
569 variation during 1100–1700 KST, weakened under LD conditions, suggesting that the shape of  
570 the NO<sub>2</sub> profile typically deviates from a uniform profile under SD and MD conditions. Aircraft  
571 measurements under LD conditions demonstrated NO<sub>2</sub> plumes aloft, with anomalous vertical  
572 structures and different horizontal (latitudinal) gradients of surface NO<sub>2</sub> at higher altitudes,  
573 such as 600 m over Seosan.

574 Thus, the relationship between PC-NO<sub>2</sub> and SI-NO<sub>2</sub> depends on the presence of NO<sub>2</sub>  
575 plumes aloft under LD conditions, which provide a favorable environment for LPS plumes  
576 decoupled from the surface at Seosan. Our findings suggest that the correlation between PC-  
577 NO<sub>2</sub> and SI-NO<sub>2</sub> may serve as an indicator of the degree of complexity of urban air quality.  
578 This correlation can be optimally applied for air quality evaluation and vertical analysis by  
579 combining the Pandora Asia Network with AQM networks, and the results can be also applied



580 to environmental GEMS observation analysis in combination with SI observations. More  
581 detailed studies on urban air pollution evaluation will be undertaken based on PC, DOAS,  
582 aircraft, SI air quality, and surface turbulence observation data, as well as modeling studies of  
583 data collected during the GMAP-2021 campaign.

584

#### 585 **Acknowledgments**

586 We thank all those who contributed to the GMAP-2020 field campaign, NASA GSFC for use of Pandora  
587 instruments, and PGN for raw data processing.

588

#### 589 **Funding.**

590 This study was supported by the National Institute of Environmental Research (NIER-2021-01-01-052  
591 and NIER-2021-03-03-001), and was partially supported by National Research Foundation of Korea  
592 (NRF) funded by the Ministry of Education of the Republic of Korea (Grant No. 2020R1I1A2075417)

593

#### 594 **Data Availability.**

595 The measurements can be accessed by contacting the corresponding authors.

596

#### 597 **Competing interest.**

598 The authors declare that they have no conflict of interest.

599

#### 600 **Author Contributions.**

601 Lim-Seok Chang: Conceptualization, Formal analysis, Visualization, Investigation, Writing -  
602 Original draft; Donghee Kim, Hyunkee Hong, Deok-Rae Kim, Jeonga Yu, and Daewon Kim; Data  
603 curation; Hanlim Lee, Kwangyul Lee, and Jinkyu Hong: Methodology and formal analysis; Hyun-

604 Young Jo: Formal analysis and Visualization; Cheol-Hee Kim ; Writing—original draft preparation,  
605 Writing—review and editing. All authors have read and agreed to the published version of the  
606 manuscript.

## 607 **References**

608 Biggs, W.G. and Graves, M.E.: A lake breeze index, *J. Appl. Meteor.*, 1, 474–480,  
609 <http://www.jstor.org/stable/26169480>, 1962.

610 Boersma, K.F., Jacob, D.J., Trainic, M., Rudich, Y., DeSmedt, I., Dirksen, R., and Eskes, H.J.:  
611 Validation of urban NO<sub>2</sub> concentrations and their diurnal and seasonal variations observed from the  
612 SCIAMACHY and OMI sensors using in situ surface measurements in Israeli cities. *Atmos. Chem.*  
613 *Phys.*, 9, 3867–3879, <https://doi.org/10.5194/acp-9-3867-2009>, 2009.

614 Cede A.: Manual for Blick Software Suite 1.7, Tech. rep., LuftBlick, Austria, 161 pp., 2019.

615 Chong, H., Lee, H., Koo, J.H., Kim, J., Jeong, U., Kim, W., Kim, S.W., Herman, J.R., Abuhassan, N.K.,  
616 Ahn, J.Y., Park, J.H., Kim, S.K., Moon, K.J., Choi, W.J., and Park, S.S.: Regional characteristics  
617 of NO<sub>2</sub> column densities from Pandora observations during the MAPS-Seoul campaign, *Aerosol*  
618 *Air Qual. Res.* 18, 2207–2219, <https://doi.org/10.4209/aaqr.2017.09.0341>, 2018.

619 Engel-Cox, J.A., Holloman, C.H., Coutant, B.W., and Hoff, R.M.: Qualitative and quantitative  
620 evaluation of MODIS satellite sensor data for regional and urban scale air quality, *Atmos. Environ.*,  
621 38, 2495–2509, <http://dx.doi.org/10.1016/j.atmosenv.2004.01.039>, 2004.

622 Flynn, C.M., Pickering, K.E., Crawford, J.H., Weinheimer, A.J., Diskin, G., Thornhill, K.L., Loughner,  
623 C., Lee, P., and Strode, S.A.: Variability of O<sub>3</sub> and NO<sub>2</sub> profile shapes during DISCover-AQ:  
624 Implications for satellite observations and comparisons to model-simulated profiles, *Atmos.*  
625 *Environ.*, 147, 133–156, <https://doi.org/10.1016/j.atmosenv.2016.09.068>, 2016.

626 Herman, J., Cede, A., Spinei, E., Mount, G., Tzortziou, M., and Abuhassan, N.: NO<sub>2</sub> column amounts  
627 from ground-based Pandora and MFDOAS spectrometers using the direct-sun DOAS technique:

628 Intercomparisons and application to OMI validation, *J. Geophys. Res. Atmos.*, 114, D13307,  
629 <https://doi.org/10.1029/2009JD011848>, 2009.

630 Herman, J., Spinei, E., Fried, A., Kim, J., Kim, J., Kim, W., Cede, A., Abuhassan, N., and Rozenhaimer,  
631 S.M.: NO<sub>2</sub> and HCHO measurements in Korea from 2012 to 2016 from Pandora spectrometer  
632 instruments compared with OMI retrievals and with aircraft measurements during the KORUS-AQ  
633 campaign, *Atmos. Meas. Tech.*, 11, 4583–4603, <https://doi.org/10.5194/amt-11-4583-2018>, 2018.

634 Hong, J.-W., Lee, S.-D., Lee, K., and Hong, J.: Seasonal variations in the surface energy and CO<sub>2</sub> flux  
635 over a high-rise, high-population, residential urban area in the East Asian monsoon region, *Int. J.*  
636 *Climatol.*, 40, 4384–4407, <https://doi.org/10.1002/joc.6463>, 2019.

637 Jo, H.-Y. and Kim, C.-H: Identification of long-range transported haze phenomena and their  
638 meteorological features over Northeast Asia, *J. Appl. Meteorol. Climatol.*, 52(6), 1318–1328,  
639 <https://doi.org/10.1175/JAMC-D-11-0235.1>, 2013.

640 Kim, C.-H., Lee, H.-J., Kang, J.-E., Jo, H.-Y., Park, S.-Y., Jo, Y.-J., Lee, J.-J., Yang, G.-H., Park, T.,  
641 and Lee, T.: Meteorological Overview and Signatures of Long-range Transport Processes during  
642 the MAPS-Seoul 2015 Campaign, *Aerosol Air Qual. Res.*, 18, 2173–2184,  
643 <https://doi.org/10.4209/aaqr.2017.10.0398>, 2018.

644 Kim, C.-H., Park, S.-Y., Kim, Y.-J., Chang, L.-S., Song, S.-K., Moon, Y.-S., and Song, C.-K.: A  
645 Numerical Study on Indicators of Long-range Transport Potential for Anthropogenic Particle Matter  
646 over Northeast Asia, *Atmos. Environ.*, 58, 35–44, <https://doi.org/10.1016/j.atmosenv.2011.11.002>,  
647 2012.

648 Kim, J., Jeong, U., Ahn, M.-H., Park, R.J., Lee, H., Song, C.H., Choi, Y.-S., Lee, K.-H. Yoo, J.-M.,  
649 Jeong, M.-J. Park, S.K., Lee, K.-M., Song, C.-K., Kim, S.-W., Kim, Y.J., Kim, S.-W., Kim, M., Go,  
650 S., Liu, X., Chance, K., Miller, C.C., Al-Saadi, J., Veihelmann, B., Bhartia, P.K., Torres, O., Abad,  
651 G.G., Haffner, D.P., Ko, D.H., Lee, S.H., Woo, J.-H., Chong, H., Park, S.S., Micks, D., Choi, W.J.,  
652 Moon, K.-J., Veefkind, P., Levelt, P.F., Edwards, D.P., Kang, M., Eo, M., Bak, J., Baek, K., Kwon,

653 H.-A., Yang, J., Park, J., Han, K.M., Kim, B.-R., Shin, H.-W., Choi, H., Lee, E., Chong, J., Cha, Y.,  
654 Koo, J.-H., Hayashida, S., Kasai, Y., Kanaya, Y., Liu, C., Lin, J., Crawford, J.H., Carmichael, G.R.,  
655 Newchurch, M.,J., Lefer, B.L., Herman, J.R., Swap, R.J., Lau, A.K.H., Kurosu, T.P., Jaross, G.,  
656 Ahlers, B., Dobber, M., McElroy, T.C., and Choi, Y.: New era of air quality monitoring from space:  
657 Geostationary Environment Monitoring Spectrometer (GEMS), *Bulletin of the American*  
658 *Meteorological Society*, 101(1), E1-E22, <https://doi.org/10.1175/BAMS-D-18-0013.1>, 2020.

659 Kim, S.-U., Kim, K.-Y.: Physical and chemical mechanisms of the daily-to-seasonal variation of PM<sub>10</sub>  
660 in Korea. *Sci. Total Environ.*, 712, 136429, <https://doi.org/10.1016/j.scitotenv.2019.136429>, 2020.

661 Kim, S.-M., Koo, J.-H., Lee, H., Mok, J., Choi, M., Go, S., Lee, S., Cho, Y., Hong, J., and Seo, S.:  
662 Comparison of PM<sub>2.5</sub> in Seoul, Korea Estimated from the Various Ground-Based and Satellite AOD,  
663 *Appl. Sci.*, 11(22), 10755, <https://doi.org/10.3390/app112210755>, 2021.

664 Lamsal, L.N., Martin, R.V., van Donkelaar, A., Celarier, E.A., Bucsela, E.J., Boersma, K.F., Dirksen,  
665 R., Luo, C., and Wang, Y.: Indirect validation of tropospheric nitrogen dioxide retrieved from the  
666 OMI satellite instrument: Insight into the seasonal variation of nitrogen oxides at northern  
667 midlatitudes, *J. Geophys. Res.*, 115, D05302, <https://doi.org/10.1029/2009JD013351>, 2010.

668 Lee, S., Kim, M., Kim, S.Y., Lee, D.W., Lee, H., Kim, J., Le, S., and Liu, Y.: Assessment of long-range  
669 transboundary aerosols in Seoul, South Korea from Geostationary Ocean Color Imager (GOCI) and  
670 ground-based observations, *Environ. Pollut.*, 269, 115924,  
671 <https://doi.org/10.1016/j.envpol.2020.115924>, 2021.

672 Lee, S.J., Lee, J., Greybush, S.J., Kang, M., and Kim, J.: Spatial and temporal variation in PBL height  
673 over the Korean Peninsula in the KMA operational regional model, *Adv. Meteorol.*, 2013(10), 1-  
674 16, <https://doi.org/10.1155/2013/381630>, 2013.

675 National Institute of Environmental Research (NIER): Air Quality Monitoring Network Installation and  
676 Operation. Ministry of the Environment, Seoul, Korea, 2021.

677 Sanchez, M.L., Pascual, D., Ramos, C. and Perez, I.: Forecasting particulate pollutant concentrations in

678 a city from meteorological variables and regional weather patterns, *Atmos. Environ.*, 6, 1509–1519,  
679 [https://doi.org/10.1016/0960-1686\(90\)90060-Z](https://doi.org/10.1016/0960-1686(90)90060-Z), 1990.

680 Stohl, A., Eckhardt, S., Forster, C., James, P., and Spichtinger, N.: On the pathways and timescales of  
681 intercontinental air pollution transport, *J. Geophys. Res.*, 107(D23), 4684,  
682 doi:10.1029/2001JD001396, 2002.

683 Sun, J., Lenschow, D.H., Mahrt, L., and Nappo, C.: The relationships among wind, horizontal pressure  
684 gradient, and turbulent momentum transport during CASES-99, *J. Atmos. Sci.*, 70, 3397–3414,  
685 <http://dx.doi.org/10.1175/JAS-D-12-0233.1>, 2013.

686 Thompson, A.M., Stauffer, R.M., Boyle, T.P., Kollonige, D.E., Miyazaki, K., Tzortziou, M., Herman,  
687 J.R., Abuhassan, N., Jordan, C.E., and Lamb, B.T.: Comparison of near-surface NO<sub>2</sub> pollution with  
688 Pandora total column NO<sub>2</sub> during the Korea-United States Ocean Color (KORUS OC) Campaign,  
689 *J. Geophys. Res. Atmos.*, 124, 13560–13575, <https://doi.org/10.1029/2019JD030765>, 2019.

690 Van Roozendael, M. and Fayt, C.: WinDOAS Software user manual, Tech. rep., IASB/BIRA, Uccle,  
691 Belgium, <http://uv-vis.aeronomie.be/software/WinDOAS>, 2001.

692 Venkat Reddy M., Vivekananda M. and Satish RUVN: Divisive Hierarchical Clustering with K-means  
693 and Agglomerative Hierarchical Clustering, *International Journal of Computer Science Trends and*  
694 *technology*, 5(5), 6–12, doi:10.17485/ijst/2016/v9is1/96012, 2017.

695 Wang, J., and Christopher, S.A.: Intercomparison between satellite-derived aerosol optical thickness  
696 and PM<sub>2.5</sub> mass: Implications for air quality studies, *Geophys. Res. Lett.*, 30, 2095,  
697 <https://doi.org/10.1029/2003GL018174>, 2003.

698 Wang, Y., Dörner, S., Donner, S., Böhnke, S., Smedt, I.D., Dickerson, R.R., Dong, Z., He, H., Li, Z.,  
699 Li, D., Ren, X., Theys, N., Wang, Y., Wang, Z., Xu, H., Xu, J., and Wagner, T.: Vertical profiles of  
700 NO<sub>2</sub>, SO<sub>2</sub>, HONO, HCHO, CHOCHO and aerosols derived from MAX-DOAS measurements at a  
701 rural site in the central western North China Plain and their relation to emission sources and effects  
702 of regional transport, *Atmos. Chem. Phys.*, 2, 5417–5449, <http://dx.doi.org/10.5194/acp-19-5417->

703 2019, 2019.

704 Wenig, M., Spichtinger, N., Stohl, A., Held, G., Beirle, S., Wagner, T., Jahne, B., and Platt, U.:  
705 Intercontinental transport of nitrogen oxide pollution plumes, *Atmos. Chem. Phys.*, 3, 387–393,  
706 SRef-ID: 1680-7324/acp/2003-3-387, 2003.

707 Zhao, X., Griffin, D., Fioletov, V., McLinden, C., Davies, J., Ogyu, A., Lee, S. C., Lupu, A., Moran,  
708 M. D., Cede, A., Tiefengraber, M., and Müller, M.: Retrieval of total column and surface NO<sub>2</sub> from  
709 Pandora zenith-sky measurements, *Atmos. Chem. Phys.*, 19, 10619–10642,  
710 <https://doi.org/10.5194/acp-19-10619-2019>, 2019.

711

712

713

714

715

716

717

718

719

720

721

722

723

724

### List of Tables

725

726 **Table 1.** Summary of NO<sub>2</sub> column data from four Pandora (PA) measurement sites.

727 **Table 2.** Summary of aircraft measurements collected during the Geostationary Environment  
728 Monitoring Spectrometer (GEMS) Map of Air Pollution (GMAP)-2020 campaign period  
729 (November 12, 2020–January 20, 2021).

730

731

732

733

734

735

736 **Table 1.** Summary of NO<sub>2</sub> column data from four Pandora (PA) measurement sites.

Site	Site name	Site location		Mean (DU)	SD (DU)	Minimum (DU)	Maximum (DU)	Number of data points (days)	Operating period
		Longitude (°E)	Latitude (°N)						
PA <sub>1</sub>	Seosan-DHJ	126.502	36.900	0.50	0.22	0.20	1.60	838 (11)	GMAP-2020 campaign
PA <sub>2</sub>	Seosan-DM	126.458	36.778	0.43	0.19	0.18	1.62	1241 (13)	GMAP-2020 campaign
PA <sub>3</sub>	Seosan-CC	126.449	36.785	0.40	0.14	0.18	0.97	1242 (13)	GMAP-2020 campaign
PA <sub>4</sub>	Seosan-SS	127.492	36.777	0.39	0.16	0.17	1.79	8753 (141)*	1 year (Nov. 12, 2020–Oct. 30, 2021)

737 \* The Pandonia Global Network (PGN) retrieval algorithm was applied to yearly  
738 measurements.

739

740

741

742

743

744 **Table 2.** Summary of aircraft measurements collected during the Geostationary Environment  
745 Monitoring Spectrometer (GEMS) Map of Air Pollution (GMAP)-2020 campaign period  
746 (November 12, 2020–January 20, 2021).

Flight no.	Date	Meteorological classification
FL-1	Nov. 26, 2020	MD <sup>1)</sup>
FL-2	Nov. 27, 2020	No Pandora measurements
FL-3	Nov. 28, 2020	MD
FL-4	Dec. 1, 2020	LD <sup>2)</sup>
FL-5	Dec. 6, 2020	LD
FL-6	Dec. 8, 2020	LD
FL-7	Dec. 9, 2020	LD
FL-8	Dec. 12, 2020 (am)	MD
FL-9	Dec. 12, 2020 (pm)	MD

747 <sup>1)</sup> LD: local wind-dominant conditions; <sup>2)</sup> MD: mixed conditions.

748

749

750

751



752

## Figure Captions

753 **Figure 1.** Map of sites used for Geostationary Environment Monitoring Spectrometer (GEMS) Map of  
754 Air Pollution (GMAP) campaigns conducted in (left) Seosan, South Korea in November 2020 to  
755 January 2021 (GMAP-2020), and (right) the Seoul metropolitan area from October 2021 to November  
756 2021 (GMAP-2021). (Left) Measurement sites around Seosan, the study area for the GMAP-2020  
757 campaign. Red circles indicate Pandora column measurement sites including (left) Seosan Daehoji  
758 (PA<sub>1</sub>), Seosan Dongmun (PA<sub>2</sub>), Seosan City Council (PA<sub>3</sub>), and Seosan Super Site (PA<sub>4</sub>). Blue triangles  
759 indicate large point sources (LPSs) including the Taeon and Dangjin thermal power stations (LPS<sub>1</sub> and  
760 LPS<sub>2</sub>, respectively), Hyundai steelworks (LPS<sub>3</sub>), and Daesan petrochemical complex (LPS<sub>4</sub>). Yellow  
761 squares indicate Automated Synoptic Observing System meteorological sites in Seosan (Met<sub>1</sub>), AWS  
762 (Met<sub>2</sub>), and buoy (Met<sub>3</sub>). Green squares indicate air quality monitoring (AQM) network stations  
763 including Padori (AQM<sub>1</sub>), Leewon (AQM<sub>2</sub>), Taeon (AQM<sub>3</sub>), Daesan (AQM<sub>4</sub>), Seongyeon (AQM<sub>5</sub>), and  
764 Dongmoon (AQM<sub>6</sub>). In the right panel, the black line indicates the route used for car-based differential  
765 optical absorption spectroscopy (Car-DOAS) measurements and the blue dotted line indicates the  
766 horizontal domain of Geo-CAPE airborne simulator (GCAS) measurements taken during the GMAP-  
767 2021 campaign.

768

769 **Figure 2.** Flight tracks for two Cessna Grand Caravan 208 B aircraft over Pandora sites (left)  
770 PA<sub>4</sub> and (right) PA<sub>1</sub> during the GMAP-2020 campaign. Colored circles indicate airborne NO<sub>2</sub>  
771 concentration observations. Stacked circles indicate spiral flights conducted over two sites.

772

773 **Figure 3.** (a) Pandora column (PC) NO<sub>2</sub> measurements as a function of surface *in situ* (SI) NO<sub>2</sub>  
774 observations at Pandora sites PA<sub>1</sub>–PA<sub>3</sub> during the GMAP-2020 campaign and PA<sub>4</sub> during a 1-  
775 year period. A logarithmic regression model was used to evaluate the relationship between PC  
776 and SI measurements (black line). (b) Samplescatter plots of PC-NO<sub>2</sub> and SI-NO<sub>2</sub> for February  
777 24 (red) and April 21 (blue), 2021.

778

779 **Figure 4.** K-means clustering yielded three groups of cases for (a) surface NO<sub>2</sub> and (b) PC-  
780 NO<sub>2</sub>, associated with eight meteorological variables: (c) surface wind speed (Wsfc), (d) Psfc,  
781 (e) Psfc tendency (dPsfc/dt), (f) 925-hPa air temperature (T925), (g) 850-hPa wind speed  
782 (W850), (h) 850-hPa north–south wind component (NS850), (i) 850-hPa east–west wind  
783 component (EW850), and (j) 500-hPa geopotential height (GPH500). All data were de-

784 seasonalized using the 30-day moving average, except PC-NO<sub>2</sub>, for which the monthly average  
785 was used. (k) Simulated daily maximum mixing height (not directly clustered). (l) Box and  
786 whisker plots of the sea breeze index (SBI) at Seosan for the 1-year period. Red dots indicate  
787 the critical SBI (a value of 3), suggested by Biggs and Graves (1962).

788

789 **Figure 5.** (a) Scatterplots of daytime measurements at site PA<sub>4</sub> (a) PC-NO<sub>2</sub> vs. SI-NO<sub>2</sub> under  
790 all meteorological conditions and (b) PC-NO<sub>2</sub> vs. Surface  $\Delta$ NO<sub>2</sub> in each meteorological  
791 condition over a 1-year period (November 12, 2020–October 30, 2021). Here Surface  $\Delta$ NO<sub>2</sub>  
792 = SI-NO<sub>2</sub>–(30-day moving average) SI-NO<sub>2</sub>.

793

794 **Figure 6.** Box and whisker plots of diurnal variation in (a–c) PC-NO<sub>2</sub>, (d–f) SI-NO<sub>2</sub>, and (g–  
795 i) surface O<sub>3</sub> under synoptic wind-dominant (SD), mixed (MD), and local wind-dominant (LD)  
796 conditions in Seosan during a 1-year period (November 12, 2020–October 30, 2021).

797

798 **Figure 7.** Box and whisker plots of the vertical NO<sub>2</sub> and O<sub>3</sub> profiles measured by GMAP  
799 aircraft superposed with *in situ* AQMS<sub>1</sub> measurements during flights (a, b) FL-5 (December 6)  
800 and (d, e) FL-7 (December 6 and 9). Blue dashed lines are linear regression lines fitted to NO<sub>2</sub>  
801 and O<sub>3</sub> profiles within the planetary boundary layer (PBL). Black arrows indicate the simulated  
802 PBL height (PBLH) obtained from the Korea Meteorological Administration (KMA).  
803 HSYPLIT 24-h backward trajectories in Seosan are shown at altitudes of 100, 500, and 1,000  
804 m, starting at 1600 KST on November 26 and 1200 KST on December 12.

805

806 **Figure 8.** Box and whisker plots of vertical profiles obtained from GMAP aircraft superposed  
807 with *in situ* AQMS measurements for (1) NO<sub>2</sub> and (2) O<sub>3</sub> for flights (a) FL-1 (November 26),  
808 (b) FL-3 (November 28), and (c) FL-8 (December 12). Blue dashed lines are linear regression  
809 lines fitted to NO<sub>2</sub> and O<sub>3</sub> in the PBL. Black arrows indicate PBLH simulated by the Hybrid  
810 Single-Particle Lagrangian Integrated Trajectory (HYSPLIT) Global Forecast System (GFS).

811

812 **Figure 9.** Time series and scatterplots of PC-NO<sub>2</sub> and SI-NO<sub>2</sub> at PA<sub>2</sub> on (a) December 6, (b)  
813 December 9, (c) November 26, and (d) December 12. (e) Scatterplot of PC-NO<sub>2</sub> and SI-NO<sub>2</sub>  
814 on December 6 (blue), December 9 (red), November 26 (gray), and December 12 (black). (f)  
815 Vertical potential temperature profiles on December 6, 9, and 12, 2020. Radiosonde data for  
816 November 26, 2020 are missing.

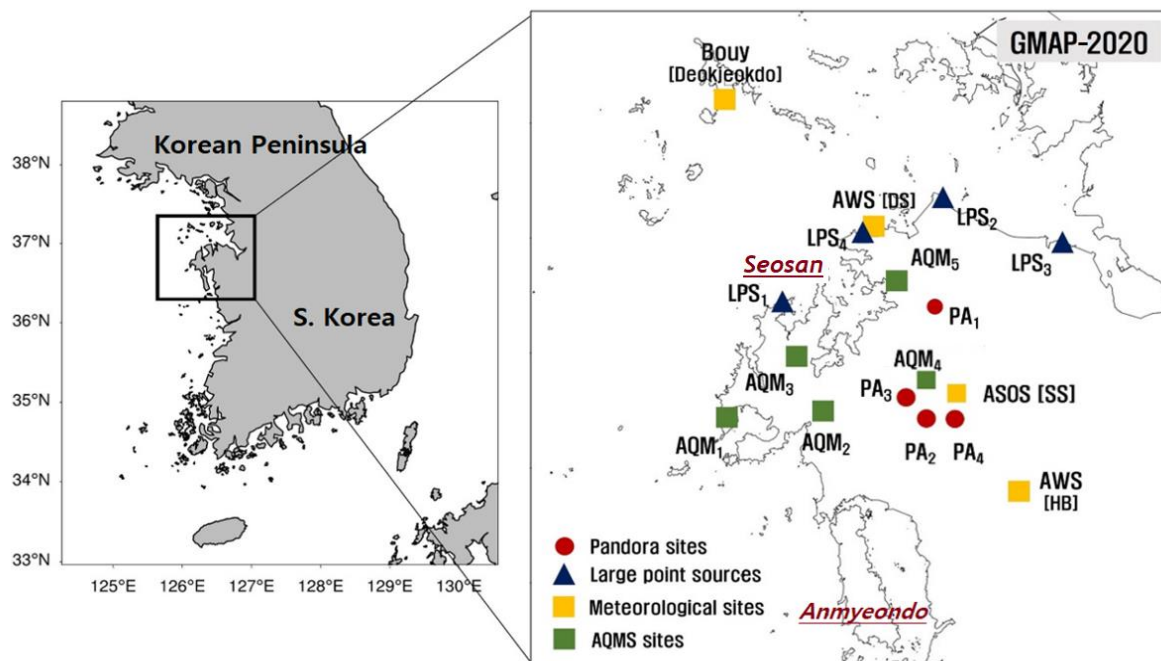
817  
818  
819  
820  
821  
822  
823  
824  
825  
826  
827  
828  
829  
830  
831  
832  
833  
834  
835  
836  
837  
838  
839  
840  
841  
842  
843

**Figure 10.** Latitudinal NO<sub>2</sub> distribution at the surface and 600 m over PA<sub>4</sub> (Seosan Super Site), averaged during (a) 1300–1600 KST on December 6 (FL-5) by longitude and (b) 1200–1400 KST on December 9 (FL-7) by latitude, obtained from airborne (blue) and surface measurements (red).

**Figure 11.** Examples of the diurnal variation on November 25 (a, c, e) and December 14 (b, d, f). (a, b) Column NO<sub>2</sub> at sites PA<sub>1</sub>–PA<sub>4</sub> and surface NO<sub>2</sub> at air quality monitoring sites AQM<sub>4</sub> and AQM<sub>6</sub>. (c, d) Sensible heat fluxes and surface wind speed at PA<sub>4</sub>. (e, f) Diurnal variation in NO<sub>2</sub>, NO<sub>2</sub><sup>-</sup>, and O<sub>3</sub> normalized by CO. Figure 1 shows the locations of the measurement sites.

844

845



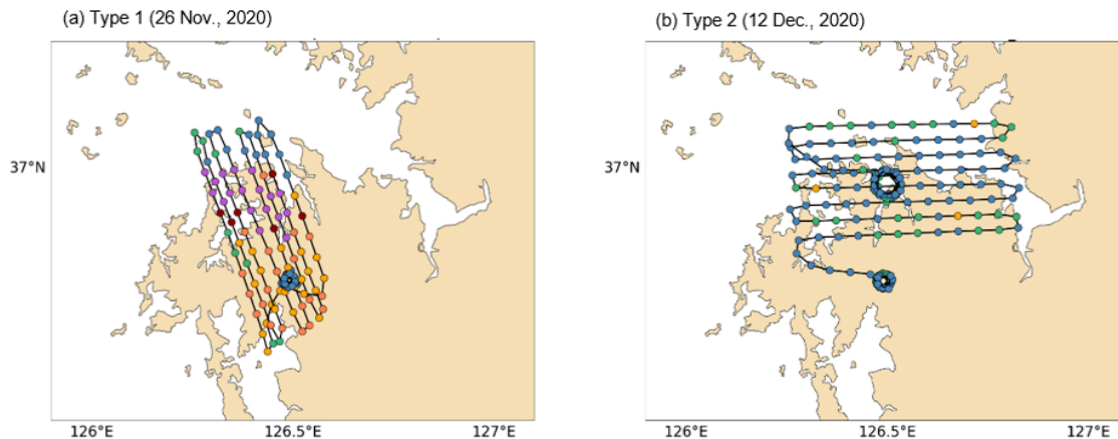
846

847 **Figure 1.** Map of sites used for Geostationary Environment Monitoring Spectrometer (GEMS) Map of  
848 Air Pollution (GMAP) campaigns conducted in (left) Seosan, South Korea in November 2020 to  
849 January 2021 (GMAP-2020), and (right) the Seoul metropolitan area from October 2021 to November  
850 2021 (GMAP-2021). (Left) Measurement sites around Seosan, the study area for the GMAP-2020  
851 campaign. Red circles indicate Pandora column measurement sites including (left) Seosan Daehoji  
852 (PA<sub>1</sub>), Seosan Dongmun (PA<sub>2</sub>), Seosan City Council (PA<sub>3</sub>), and Seosan Super Site (PA<sub>4</sub>). Blue triangles  
853 indicate large point sources (LPSs) including the Taean and Dangjin thermal power stations (LPS<sub>1</sub> and  
854 LPS<sub>2</sub>, respectively), Hyundai steelworks (LPS<sub>3</sub>), and Daesan petrochemical complex (LPS<sub>4</sub>). Yellow  
855 squares indicate Automated Synoptic Observing System meteorological sites in Seosan (Met<sub>1</sub>), AWS  
856 (Met<sub>2</sub>), and buoy (Met<sub>3</sub>). Green squares indicate air quality monitoring (AQM) network stations  
857 including Padori (AQM<sub>1</sub>), Leewon (AQM<sub>2</sub>), Taean (AQM<sub>3</sub>), Daesan (AQM<sub>4</sub>), Seongyeon (AQM<sub>5</sub>), and  
858 Dongmoon (AQM<sub>6</sub>). In the right panel, the black line indicates the route used for car-based differential  
859 optical absorption spectroscopy (Car-DOAS) measurements and the blue dotted line indicates the  
860 horizontal domain of Geo-CAPE airborne simulator (GCAS) measurements taken during the GMAP-  
861 2021 campaign.

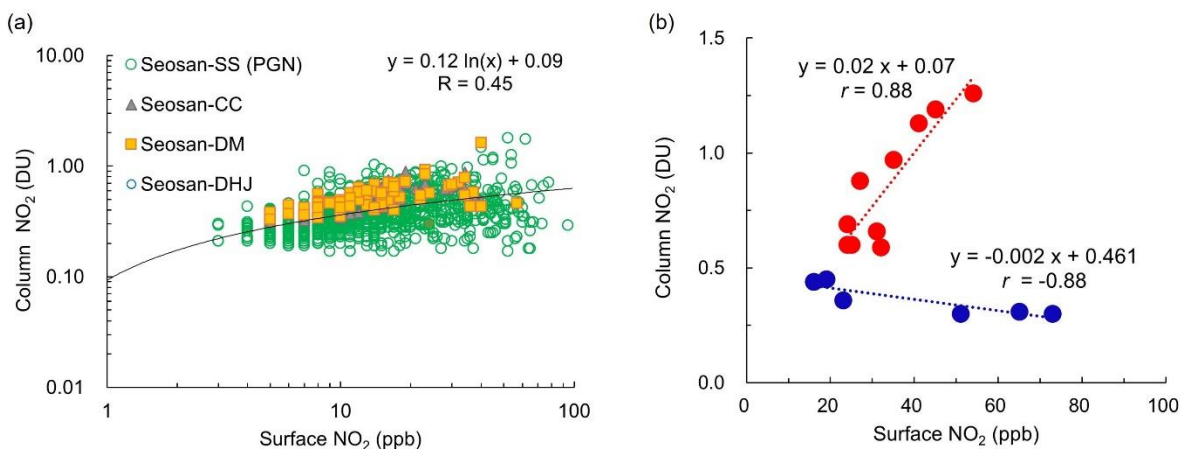
862

863

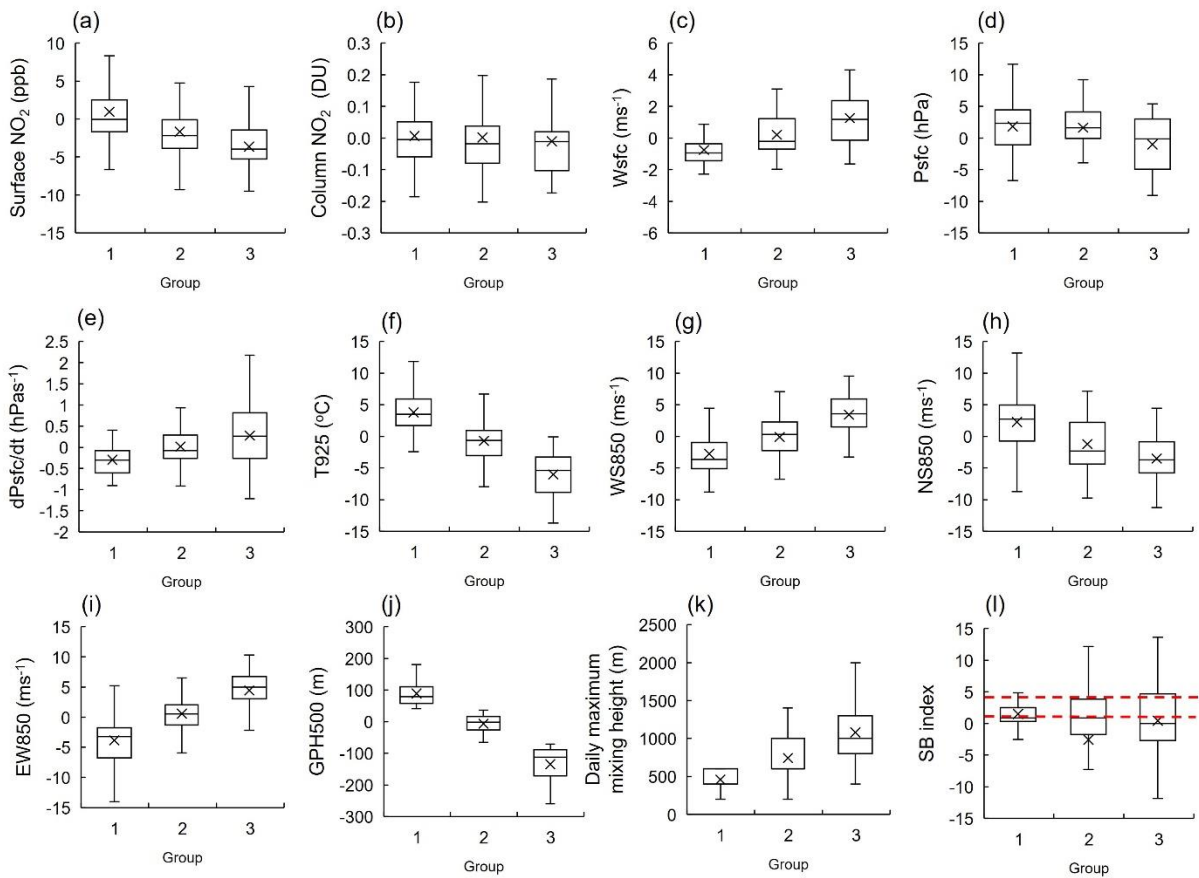
864



865  
 866 **Figure 2.** Flight tracks for two Cessna Grand Caravan 208 B aircraft over Pandora sites (left)  
 867 PA<sub>4</sub> and (right) PA<sub>1</sub> during the GMAP-2020 campaign. Colored circles indicate airborne NO<sub>2</sub>  
 868 concentration observations. Stacked circles indicate spiral flights conducted over two sites.  
 869  
 870  
 871



872  
 873 **Figure 3.** a) Pandora column (PC) NO<sub>2</sub> measurements as a function of surface *in situ* (SI) NO<sub>2</sub>  
 874 observations at Pandora sites PA<sub>1</sub>–PA<sub>3</sub> during the GMAP-2020 campaign and PA<sub>4</sub> during a 1-  
 875 year period. A logarithmic regression model was used to evaluate the relationship between PC  
 876 and SI measurements (black line). (b) Sample scatterplots of PC-NO<sub>2</sub> and SI-NO<sub>2</sub> for February  
 877 24 (red) and April 21 (blue), 2021.



879 **Figure 4.** K-means clustering yielded three groups of cases for (a) surface  $\text{NO}_2$  and (b) PC-  
 880  $\text{NO}_2$ , associated with eight meteorological variables: (c) surface wind speed (Wsfsc), (d) Psfc,  
 881 (e) Psfc tendency ( $d\text{Psfc}/dt$ ), (f) 925-hPa air temperature (T925), (g) 850-hPa wind speed  
 882 (W850), (h) 850-hPa north-south wind component (NS850), (i) 850-hPa east-west wind  
 883 component (EW850), and (j) 500-hPa geopotential height (GPH500). All data were de-  
 884 seasonalized using the 30-day moving average, except PC- $\text{NO}_2$ , for which the monthly average  
 885 was used. (k) Simulated daily maximum mixing height (not directly clustered). (l) Box and  
 886 whisker plots of the sea breeze index (SBI) at Seosan for the 1-year period. Red dots indicate  
 887 the critical SBI (a value of 3), suggested by Biggs and Graves (1962).

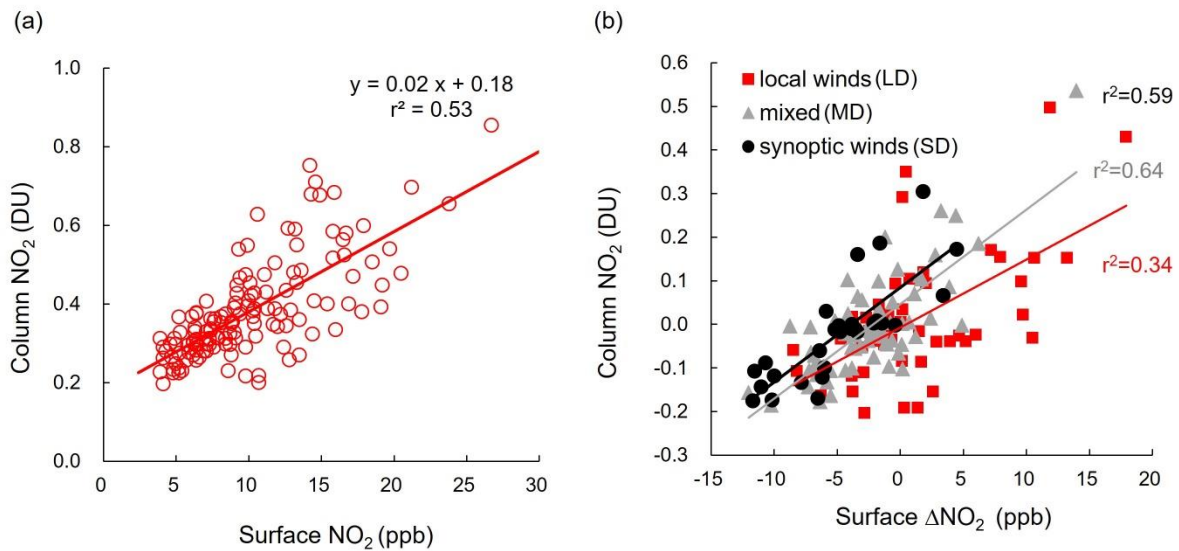
888

889

890

891

892



893

894 **Figure 5.** (a) Scatterplots of daytime measurements at site PA<sub>4</sub> (a) PC-NO<sub>2</sub> vs. SI-NO<sub>2</sub> under  
 895 all meteorological conditions and (b) PC-NO<sub>2</sub> vs. Surface  $\Delta$ NO<sub>2</sub> in each meteorological  
 896 condition over a 1-year period (November 12, 2020–October 30, 2021). Here Surface  $\Delta$ NO<sub>2</sub>  
 897 = SI-NO<sub>2</sub> – (30-day moving average) SI-NO<sub>2</sub>.

898

899

900

901

902

903

904

905

906

907

908

909

910

911

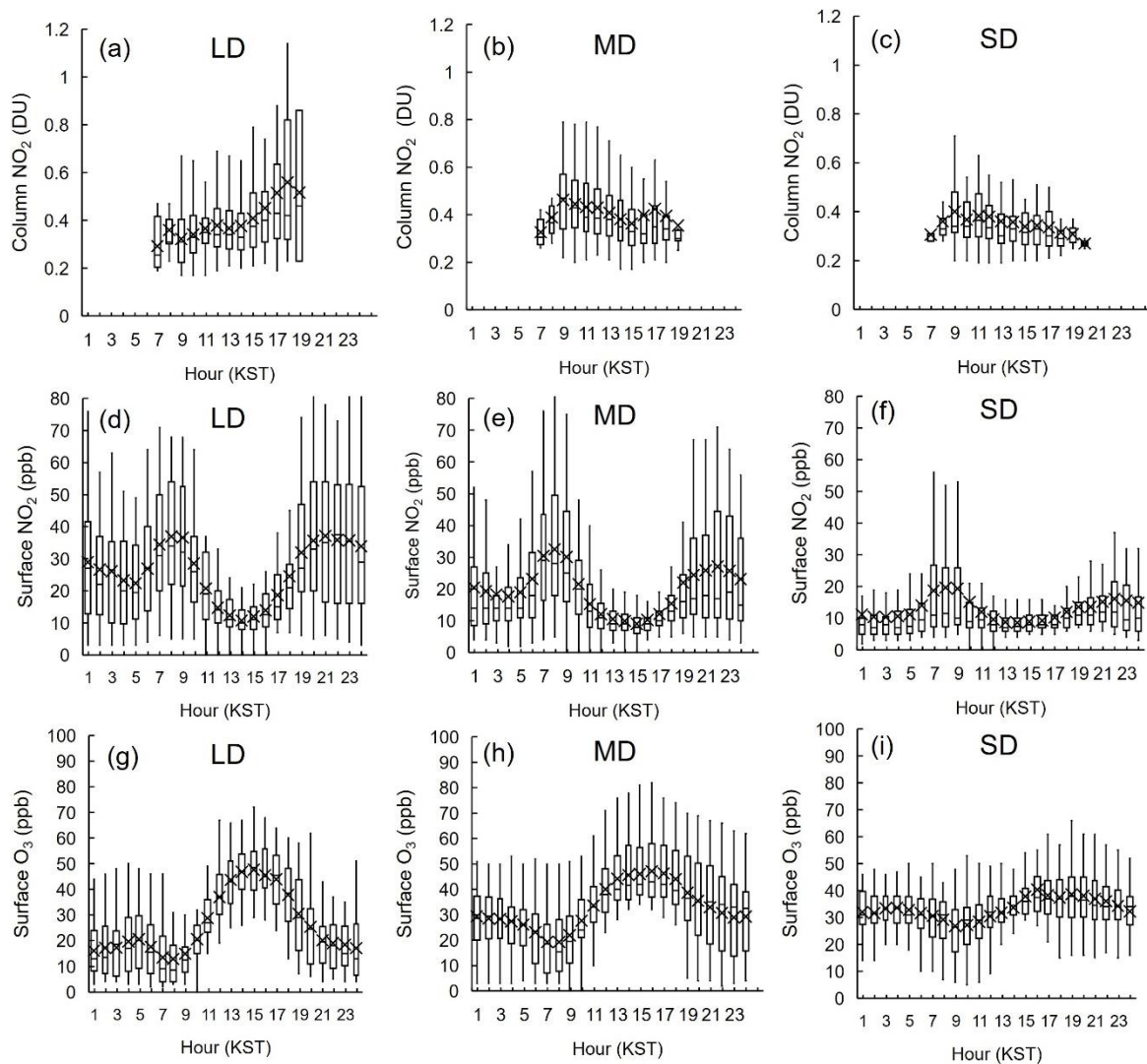
912

913

914

915





916

917 **Figure 6.** Box and whisker plots of diurnal variation in (a–c) PC-NO<sub>2</sub>, (d–f) SI-NO<sub>2</sub>, and (g–  
 918 i) surface O<sub>3</sub> under synoptic wind-dominant (SD), mixed (MD), and local wind-dominant (LD)  
 919 conditions in Seosan during a 1-year period (November 12, 2020–October 30, 2021).

920

921

922

923

924

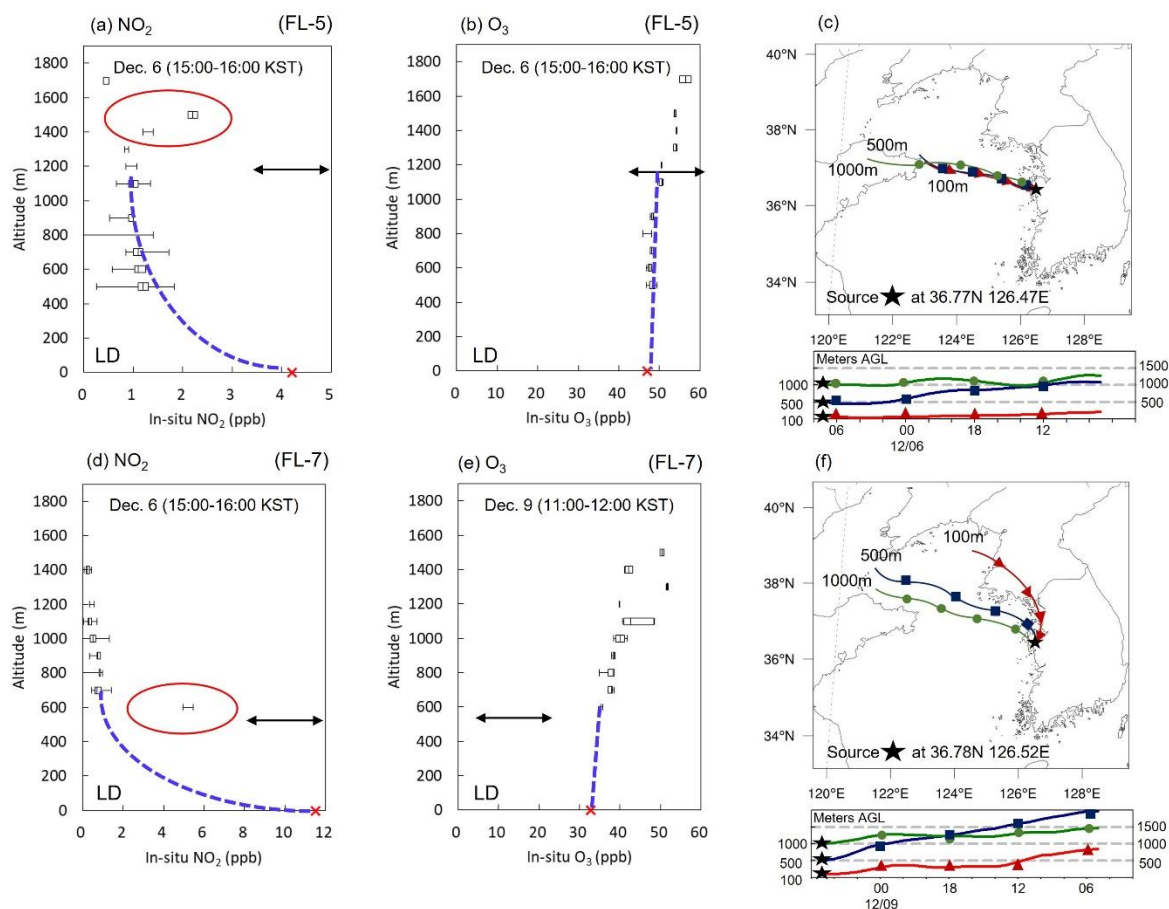
925

926



927

928



929

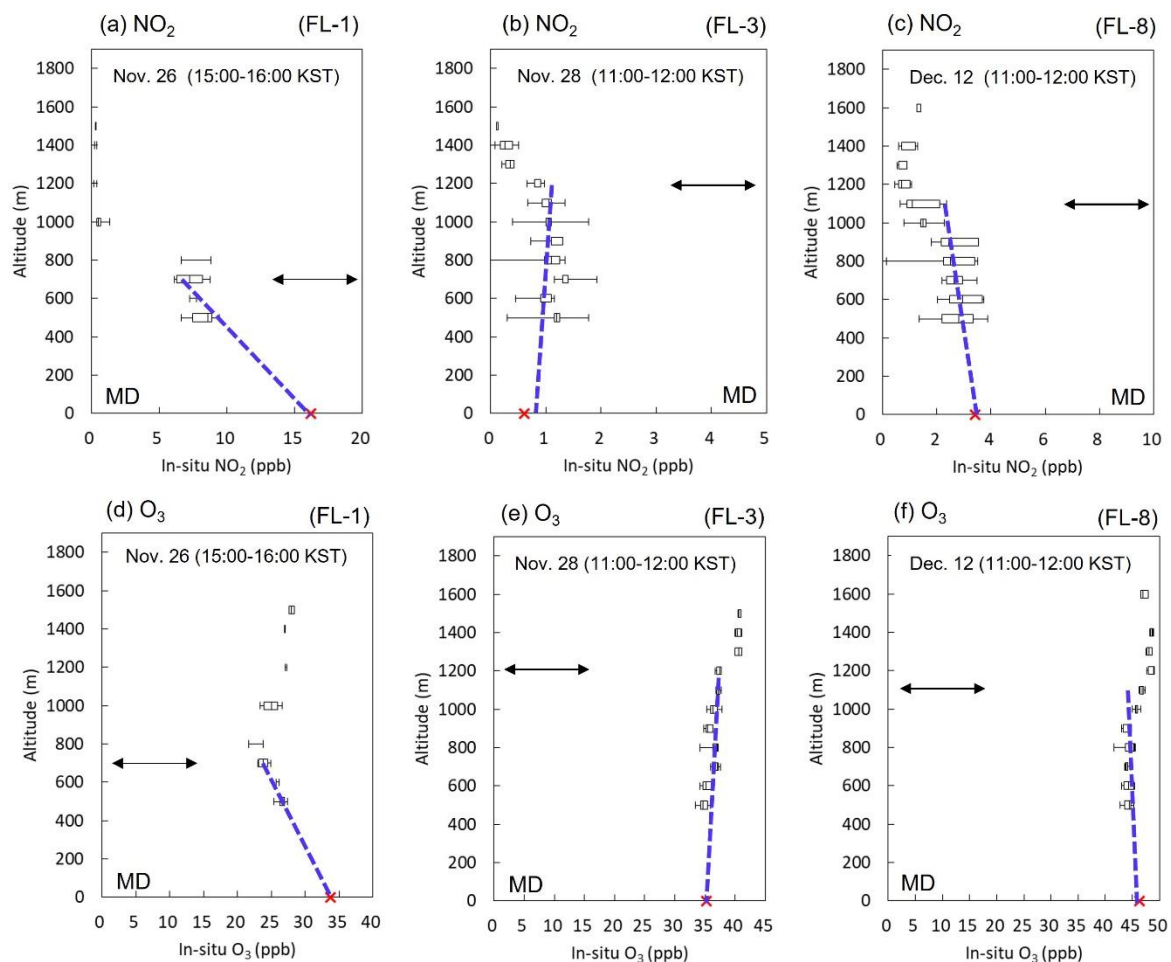
930 **Figure 7.** Box and whisker plots of the vertical NO<sub>2</sub> and O<sub>3</sub> profiles measured by GMAP  
931 aircraft superposed with *in situ* AQMS<sub>1</sub> measurements during flights (a, b) **FL-5 (December 6)**  
932 **and (d, e) FL-7 (December 6 and 9)**. Blue dashed lines are linear regression lines fitted to NO<sub>2</sub>  
933 and O<sub>3</sub> profiles within the planetary boundary layer (PBL). Black arrows indicate the simulated  
934 PBL height (PBLH) obtained from the Korea Meteorological Administration (KMA).  
935 HSYPLIT 24-h backward trajectories in Seosan are shown at altitudes of 100, 500, and 1,000  
936 m, starting at 1600 KST on November 26 and 1200 KST on December 12.

937

938

939

940



942

943 **Figure 8.** Box and whisker plots of vertical profiles obtained from GMAP aircraft superposed  
 944 with *in situ* AQMS measurements for (1) NO<sub>2</sub> and (2) O<sub>3</sub> for flights (a) FL-1 (November 26),  
 945 (b) FL-3 (November 28), and (c) FL-8 (December 12). Blue dashed lines are linear regression  
 946 lines fitted to NO<sub>2</sub> and O<sub>3</sub> in the PBL. Black arrows indicate PBLH simulated by the Hybrid  
 947 Single-Particle Lagrangian Integrated Trajectory (HYSPLIT) Global Forecast System (GFS).

948

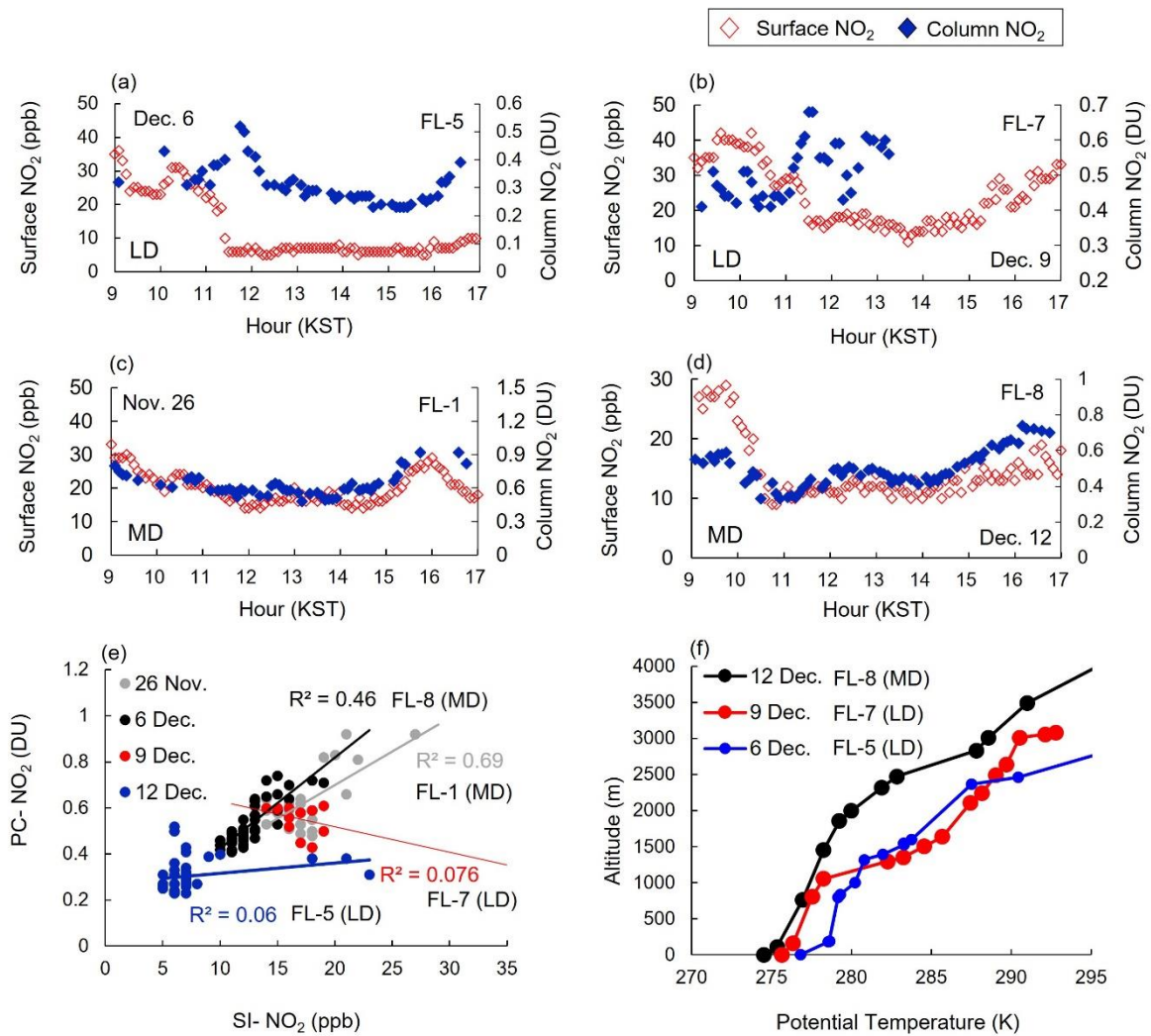
949

950

951

952

953



954

955 **Figure 9.** Time series and scatterplots of PC-NO<sub>2</sub> and SI-NO<sub>2</sub> at PA<sub>2</sub> on (a) December 6, (b)

956 December 9, (c) November 26, and (d) December 12. (e) Scatterplot of PC-NO<sub>2</sub> and SI-NO<sub>2</sub>

957 on December 6 (blue), December 9 (red), November 26 (gray), and December 12 (black). (f)

958 Vertical potential temperature profiles on December 6, 9, and 12, 2020. Radiosonde data for

959 November 26, 2020 are missing.

960

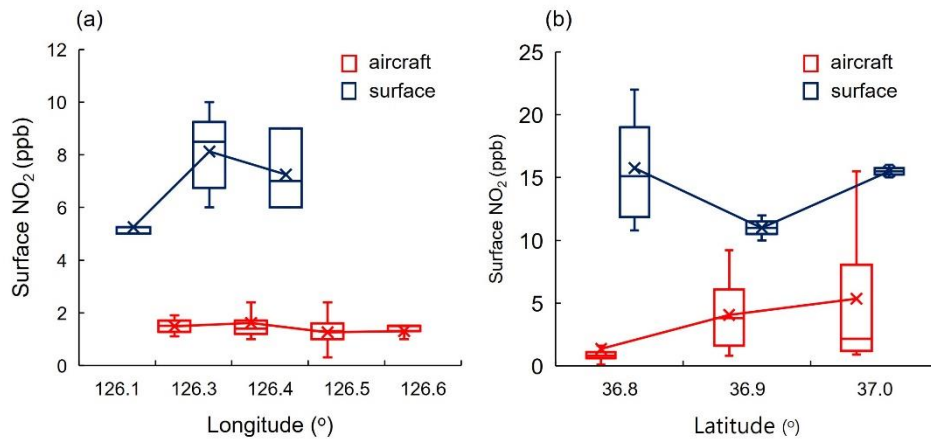
961

962

963

964

965



966

967 **Figure 10.** Latitudinal NO<sub>2</sub> distribution at the surface and 600 m over PA<sub>4</sub> (Seosan Super Site),  
 968 averaged during (a) 1300–1600 KST on December 6 (FL-5) by longitude and (b) 1200–1400  
 969 KST on December 9 (FL-7) by latitude, obtained from airborne (blue) and surface  
 970 measurements (red).

971

972

973

974

975

976

977

978

979

980

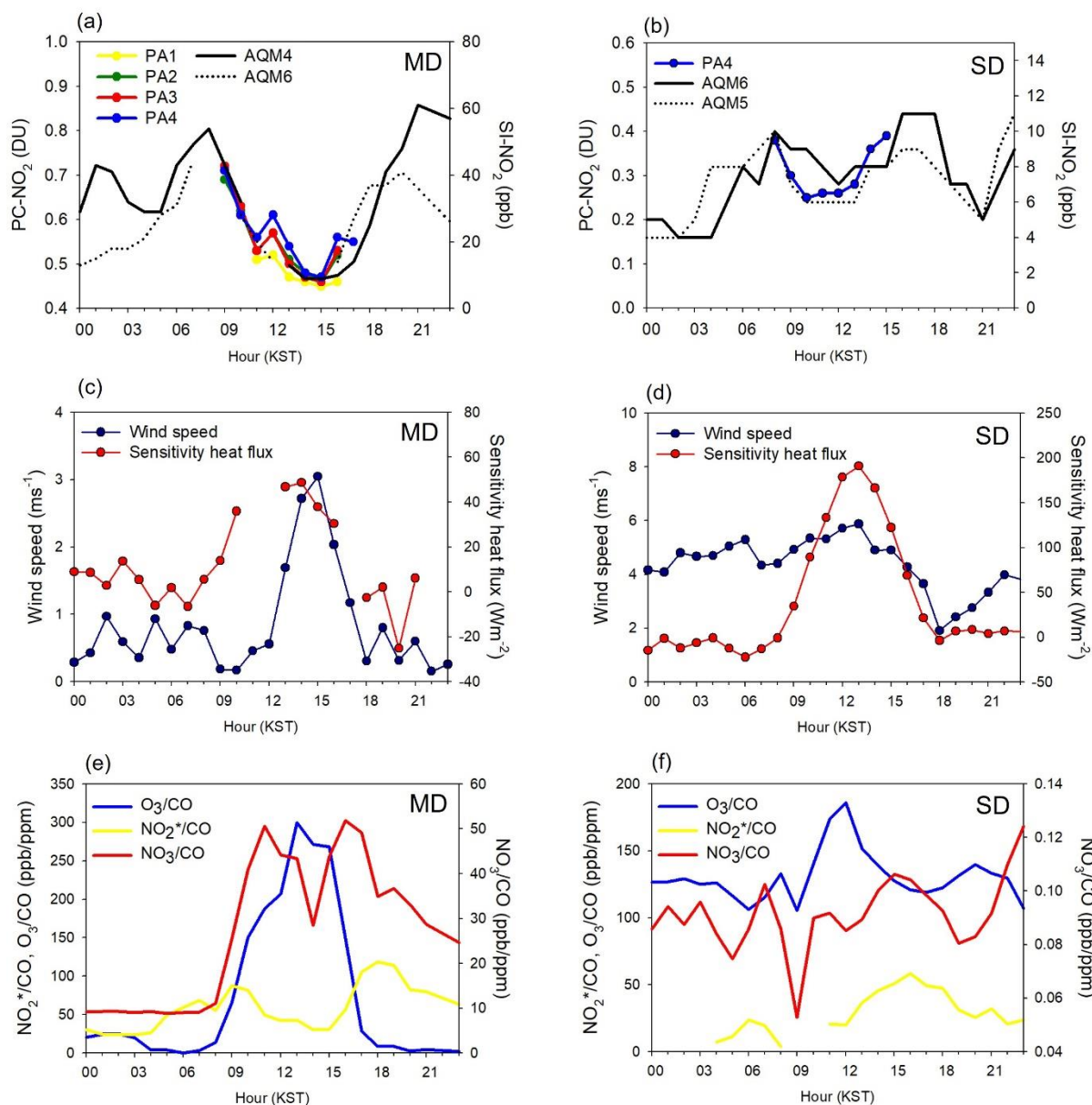
981

982

983

984

985



987

988 **Figure 11.** Examples of the diurnal variation on November 25 (a, c, e) and December 14 (b, d,  
 989 f). (a, b) Column NO<sub>2</sub> at sites PA<sub>1</sub>–PA<sub>4</sub> and surface NO<sub>2</sub> at air quality monitoring sites AQM<sub>4</sub>  
 990 and AQM<sub>6</sub>. (c, d) Sensible heat fluxes and surface wind speed at PA<sub>4</sub>. (e, f) Diurnal variation  
 991 in NO<sub>2</sub>, NO<sub>2</sub><sup>+</sup>, and O<sub>3</sub> normalized by CO. Figure 1 shows the locations of the measurement  
 992 sites.

993

994